

LIBRARY Michigan State University

This is to certify that the

thesis entitled

THE EXPERIMENTAL RESPONSE OF AN IMPACTING PENDULUM SYSTEM

presented by

Douglas Brian Moore

has been accepted towards fulfillment of the requirements for

<u>Master's</u> degree in Mechanical Engineering

Major professor

Date August 13, 1987



RETURNING MATERIALS:
Place in book drop to remove this checkout from your record. FINES will be charged if book is returned after the date stamped below.

THE EXPERIMENTAL RESPONSE OF AN IMPACTING PENDULUM SYSTEM

By

Douglas Brian Moore

A THESIS

Submitted to
Michigan State University
in partial fulfillment of the requirements
for the degree of

MASTER OF SCIENCE

Department of Mechanical Engineering

ABSTRACT

THE EXPERIMENTAL RESPONSE OF AN IMPACTING PENDULUM SYSTEM

By

Douglas Brian Moore

A simple mechanical device and its response to periodic excitation is considered. The system consists of a pendulum with rigid barriers which limit the amplitude variation from the central position. The pendulum is considered in the normal, downward position and in the upright, inverted position. The dynamics of the pendulum include impacts with the rigid constraints. When subjected to periodic excitation, the system response has been predicted to be quite complicated and may include several stable subharmonics or chaotic motions. Analytic results show the existence of bifurcations leading to the creation of subharmonic and chaotic motions [1,2,3]. Here we present the experimental verification of these analyses.

- [1] Shaw, Steven W., "The Transition to Chaos in a Simple Mechanical System", Preprint, Michigan State University, 1987.
 - [2] Shaw, Steven W., "The Dynamics of a Harmonically Excited System Having Rigid Amplitude Constraints, Part 1: Subharmonic Motions and Local Bifurcations", Transactions of the ASME Journal of Applied Mechanics, Vol. 52 1985.
 - [3] Shaw, Steven W., "The Dynamics of a Harmonically Excited System Having Rigid Amplitude Constraints, Part 2: Chaotic Motions and Global Bifurcations", Transactions of the ASME Journal of Applied Mechanics, Vol. 52 1985.

Table of Contents

List of Figures	iv
Nomenclature	v
1. Introduction	1
2. Experimental Equipment and Procedure	20
3. Results	27
3.1 Inverted Pendulum	27
3.2 Normal Pendulum	46
4. Discussion	51
Appendix A Effect of Higher Modes of Vibration on the System	5 3
Appendix B The Derivation of the Rest Solution Limit	60
Appendix C Calibration of the Hall Effect Sensor	62
References	64

List of Figures

Figure 1a	Experimental device, inverted
Figure 1b	Experimental device, normal
Figure 2a system	Phase space of unforced, undamped inverted pendulum
Figure 2b	Phase space of unforced, undamped normal pendulum sys-
	Coexistence of linear and nonlinear motion for the normal adulum, $\beta = 2.0$, $r = 0.7$, $\omega = 3.0$, $\alpha = 0$
Figure 4	Saddle-node bifurcation
Figure 5	Period doubling bifurcaton
Figure 6	Pitchfork bifurcation
Figure 7 space	Motion from saddle-node bifurcation of Type I in phase
$\beta = 0.6 ,$	$r = 1.0$, $\omega = 4.0$, $\alpha = 0.1$
Figure 8 space	Motion from saddle-node bifurcation of Type II in phase
$\beta = 2.3 ,$	$r = 1.0$, $\omega = 1.95$, $\alpha = 0.1$
space	Motion from pitchfork bifurcation of Type II in phase
$\beta = 2.3 ,$	$r = 1.0$, $\omega = 1.8$, $\alpha = 0.1$
	Motion from period doubling bifurcation of Type I in
Figure 11	Experimental equipment
Figure 12 predictions	Experimental observations of Type I motions vs.
Figure 13 predictions	Experimental observations of Type II motions vs.
Figure 14	Type I motion from a saddle-node bifurcation, period T
•	Type I motion from a saddle-node bifurcation, period 2T
Figure 16	Type I motion from a saddle-node bifurcation, period 3T
Figure 17	Type I motion from a saddle-node bifurcation, period 4T
Figure 18	Type I motion from a period doubling bifurcation, period
	Type I motion from a period doubling bifurcation, period
	Chaotic motion, angular displacement vs. time
_	Other periodic motion, inverted pendulum, period 3T, 3 er period
Figure 22	Other periodic motion, inverted pendulum, period 6T, 3

	Other periodic motion, inverted pendulum, period 12T, 3 period
Figure 24	Type II motion from a saddle-node bifurcation, period T
Figure 25	Type II motion from a saddle-node bifurcation, period 3T
Figure 26 pendulum	Experimental observations vs. predictions for normal
Figure 27	Impacting motion of normal pendulum from a saddle-node period 3T
	Impacting motion of normal pendulum from a pitchfork period 3T,
Figure 29	Other periodic motion, normal pendulum, period 9T, 6
	Simulation of shear at x=L
_	Pendulum impacts, angular velocity vs. time
•	Free body diagram of inverted pendulum at impact
Figure C1	Rotational Sensor Calibration Curve

Nomenclature

- m Mass of pendulum
- l Length of pendulum
- b Dimensional damping in pendulum bearings
- A Amplitude of input displacement
- ω_{dr} Driving frequency of input
- τ time
- θ angular displacement of pendulum
- t Nondimensional time
- φ Nondimensional angular displacement
- ω Nondimensional forcing frequency
- β Nondimensional forcing amplitude
- r Coefficient of restitution
- α Nondimensional damping ratio

1. Introduction

The development of bifurcation theory and the concept of chaos, added to classical nonlinear analysis, has allowed applied mathematicians and engineers to analyze and understand classes of problems in a new manner. Specifically, the development of the mathematical tools of dynamical systems theory have allowed engineers the opportunity to study complex systems in a more complete and rigorous manner. Inherently nonlinear systems may now be analyzed as such, allowing system response predictions to be made and providing a global understanding of the system which was not possible with linear models. These new methods have given the theoretical basis for systematic analysis and have laid the groundwork for development of design criteria for nonlinear engineering systems. Hirsch and Smale [4] provides a look at these questions from a mathematicians viewpoint, Guckenheimer and Holmes [5] look at them from a research engineering focus, and Peitgen and Richter [6] combine a graphical and artistic approach to such equations. While this thesis considers a specific nonlinear vibrations problem, the ideas and methods applied are applicable to other problems including models from biological systems to economic systems. This new way of approaching natural phenomenon, along with the generality of the methods, are what have made this experiment a rewarding study.

The system studied falls into the general class of impacting motion. Systems of this type have been studied with classical methods by Veluswami and Crossley [7], Veluswami, Crossley, and Horvay [8], Masri [9], Davies [10], and Watanbe [11] and [12]. Studies of impacting systems using bifurcation theory have been made by Shaw [1-3], Moon and Shaw [13], Shaw and Holmes [14], and Holmes [15]. The predictions and analysis used in this experiment are from Shaw [1] for

the inverted pendulum and Sharif-Bakhtiar and Shaw [16] and Shaw [2,3] for the normal pendulum.

Previous experimental work in chaotic systems has focused on showing the existence of chaos in a system or focused on subharmonic responses; typically coexistence of several motions is not considered. Studies where experiments were combined with theory include, Moon and Holmes [17], Moon, Cusumano, and Holmes [18], Moon and Shaw [13], and Shaw [19]. Theoretical developments have usually been subject only to computer simulations for verification. Here we take the theoretical predictions and computer simulations and compare them with a physical experiment.

The system considered consisted of a single degree of freedom impacting pendulum (Figures 1a, 1b). It is single degree of freedom as we are assuming the bar to be rigid. The analysis and experimental evidence to support this assumption are given in the chapter on the experimental apparatus and in Appendix A. The non-linear nature of the problem comes from the impacts at the constraints, the constraints themselves being close enough together to allow a small angle approximation to be used for the free flight dynamics. The other assumptions in the system are that the coefficient of restitution, which dictates how much energy is lost at impact, is proportional to the impact velocity, impacts are instantaneous, and the free flight damping is linear viscous in nature. The input is provided by a sinusoidal motion of the support structure.

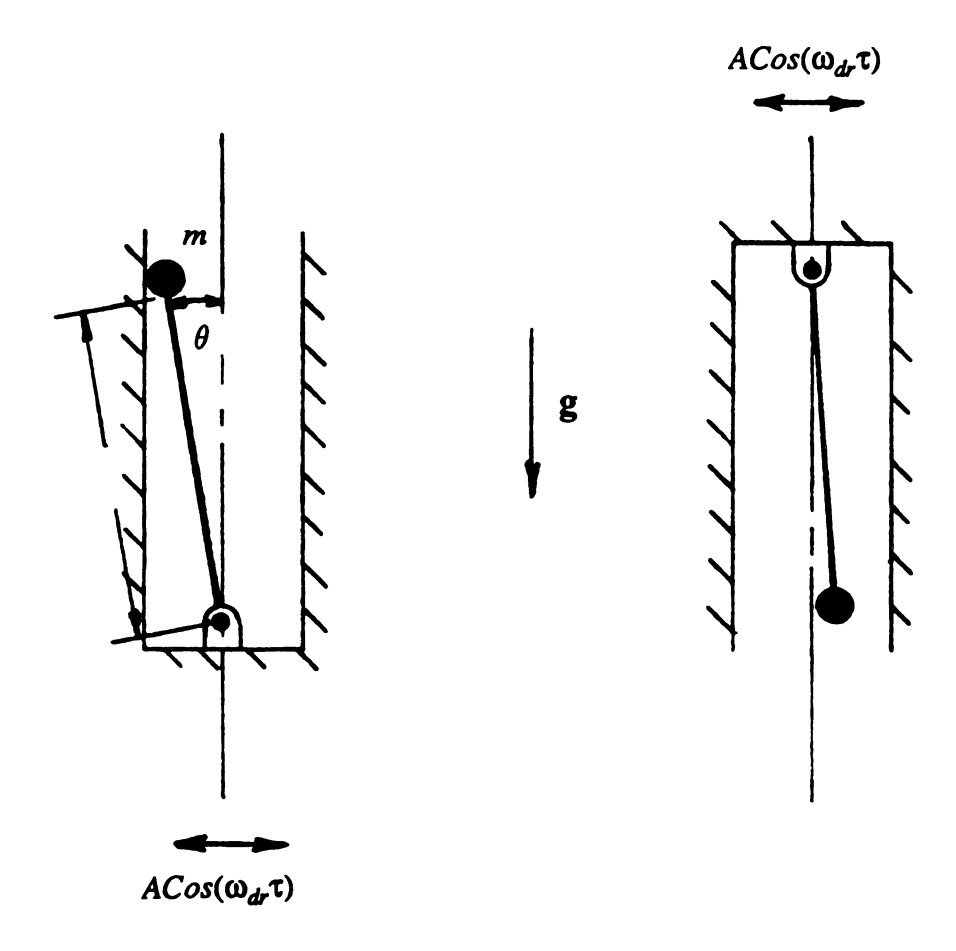


Fig. 1a Experimental device, inverted Fig. 1b Experimental device, normal

The goal in these experiments was to map out and confirm the dynamic behavior as a function of parameters of the system as predicted in [1-3] and [16]. In these papers, predictions were made for the existence and stability of certain subharmonic and chaotic motions of this system.

The thesis is arranged as follows. The remainder of Chapter 1 provides the equations of motion and a brief description of the bifurcations which lead to particular types of motion. Chapter 2 describes the experimental procedures and apparatus. Chapter 3 presents the experimental results and the observed motions and the comparison with predicted values. In Chapter 4, deviations from the

expected results are analyzed, and experimental errors and ways to improve the experiment are discussed.

The equations of motion for the impacting pendulum are as follows;

$$ml^2\theta "+b\theta '+mglSin\theta = Am\omega_{dr}^2 Cos(\omega_{dr}\tau) \qquad |\theta| < \theta_{max}$$
 (1)

$$\theta'_{+} = -r\theta'_{-} \quad |\theta| = \theta_{\text{max}} \tag{1a}$$

where m and l are the mass of the pendulum and the length of the pendulum as shown in Figures 1a and 1b. A is the amplitude of the support displacement, b is the effective angular viscous damping constant at the bearing, g is the gravitational acceleration, ω_{dr} is the frequency of the input motion, r is the coefficient of restitution at impact, and primes denote $d/d\tau$ with τ being time.

The equations of motion may be nondimensionalized by rescaling equation (1) by letting $t = \sqrt{g/l} \tau$ and $\phi = \frac{(\theta - \pi)}{(\theta_{\text{max}} - \pi)}$. The nondimensionalized equations of motion for the system depicted in Figure 1a, for small angles from the vertical $(\theta = \pi)$, are:

$$\dot{\phi} + 2 \alpha \dot{\phi} - \phi = \beta \cos (\omega t), \qquad |\phi| < 1, \quad \phi = \frac{(\theta - \pi)}{(\theta_{\text{max}} - \pi)}$$
 (2)

$$\dot{\phi}_{+} = -r\dot{\phi}_{-} \quad , \quad |\phi| = 1 \tag{2a}$$

where (') =
$$d/dt$$
, and $2\alpha = b/\sqrt{m^2l^3g}$, $\omega = \omega_{dr}\sqrt{l/g}$, and $\beta = \frac{A}{(\theta_{\text{max}} - \pi)l}(\omega_{dr}^2/g/l)$.

See [2] for details of a similar calculation. The parameter α represents the nondimensional damping ratio, β the nondimensional driving amplitude, ω the dimensionless driving frequency, and r is the coefficient of restitution. These parameters determine the dynamics of the system.

The equations for the normal (noninverted) pendulum system are similar to the equations for the inverted pendulum system. See Shaw [2,3], for analysis of these equations for a similar system. The nondimensional equations of motion for the normal pendulum are

$$\ddot{\phi} + 2 \alpha \dot{\phi} + \phi = \beta \cos(\omega t), \quad |\phi| < 1, \quad \phi = \frac{\theta}{\theta_{\text{max}}} ; \quad (3)$$

$$\dot{\phi}_{+} = -r\dot{\phi}_{-} \quad , \quad |\phi| = 1 \quad . \tag{3a}$$

The dimensionless parameters of the normal pendulum are the same as for the inverted pendulum.

The unforced, undamped phase space for the inverted and normal pendulum are given in Figures 2a and 2b, respectively.

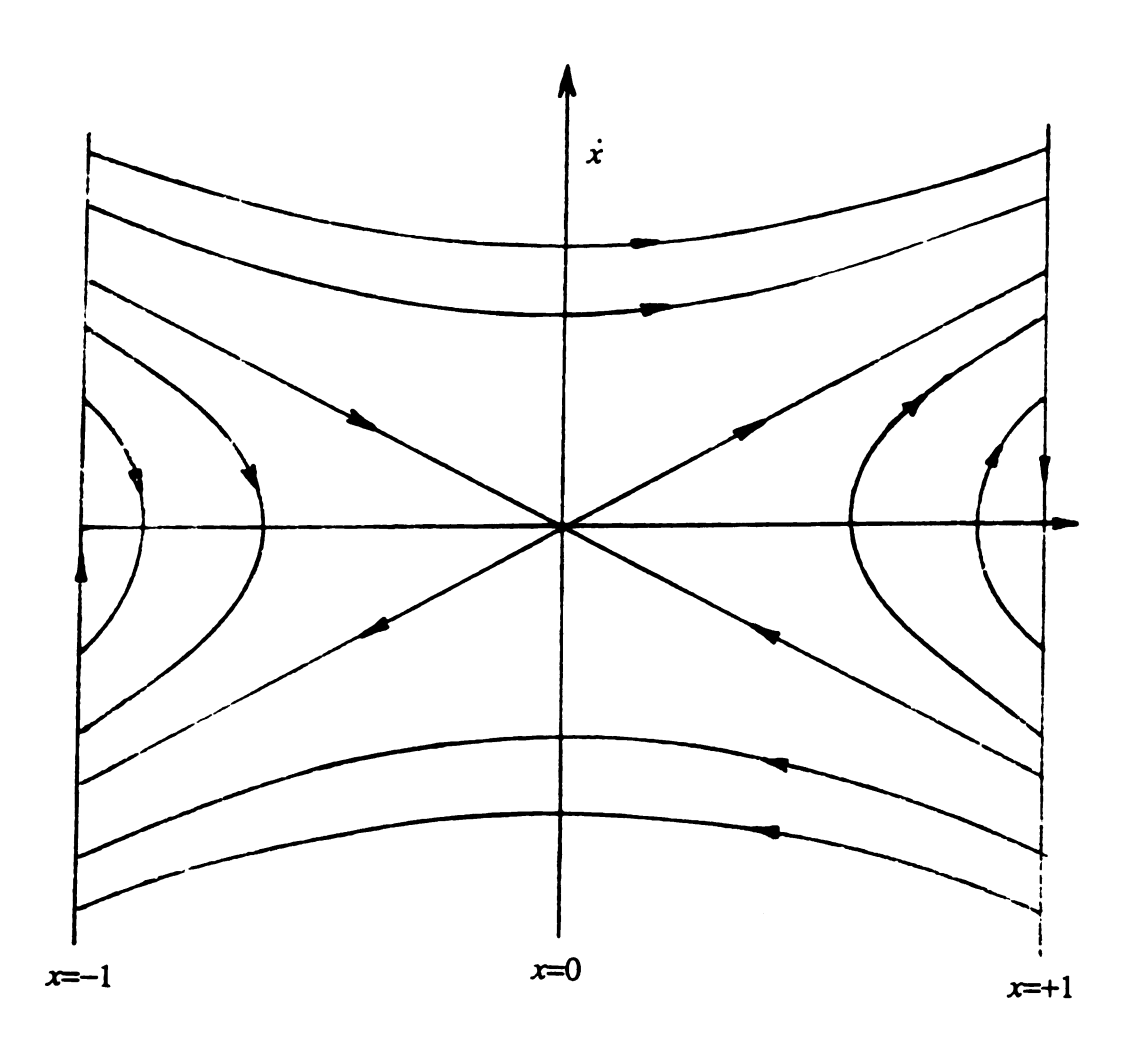


Figure 2a Phase space of unforced, undamped inverted pendulum system

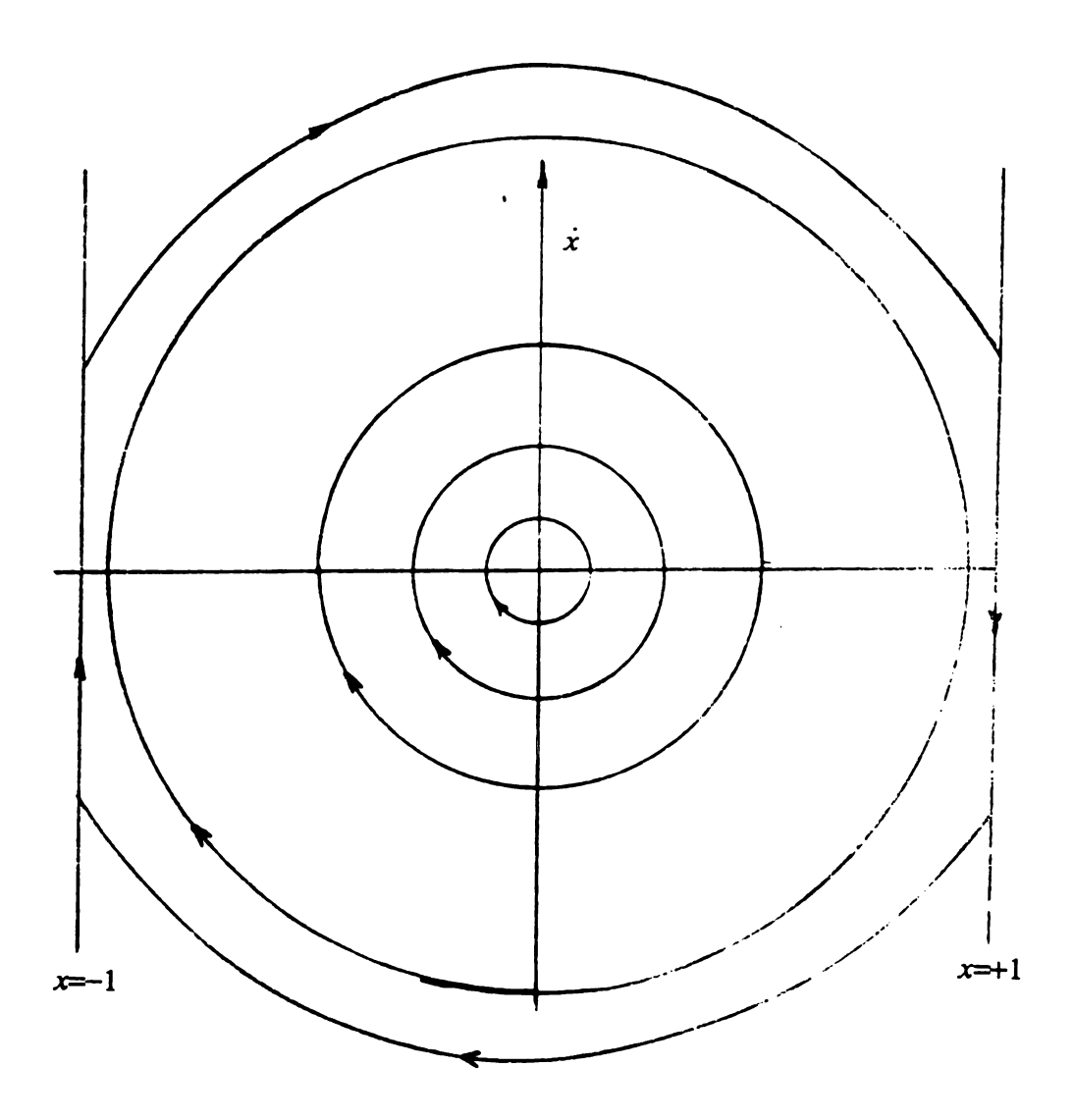


Figure 2b Phase space of unforced, undamped normal pendulum system

An interesting feature of the forced, damped normal pendulum is the possibility of coexistence of linear and nonlinear steady-state motions (Shaw [2]). Figure 3 shows an example, from simulations [2], of the coexistence of the linear nonimpacting motions and the nonlinear impacting motions in the phase space. The condition for the linear motion to exist, for $\alpha = 0$, is given by

$$\beta < |1 - \omega^2| . \tag{4}$$

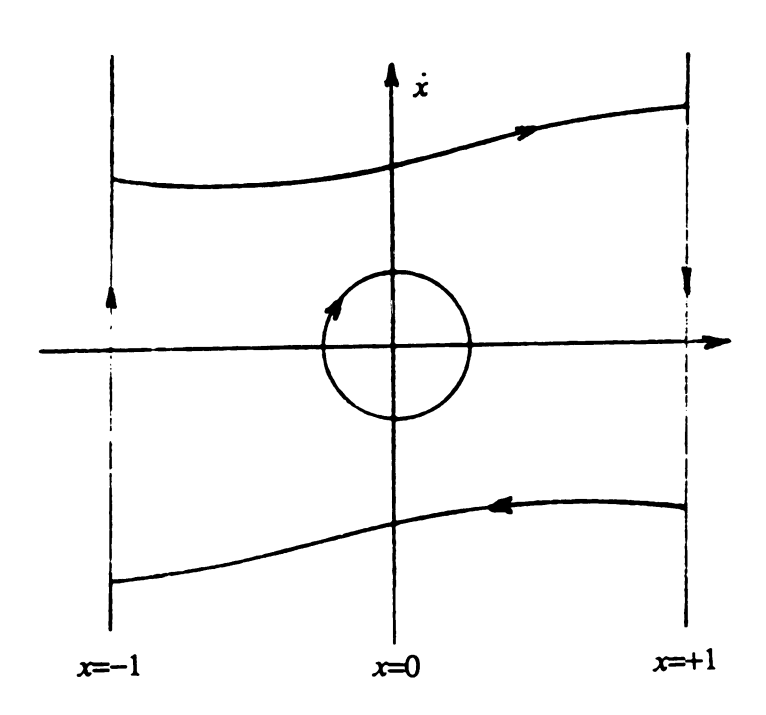


Figure 3 Coexistence of linear and nonlinear motion for the normal forced pendulum, $\beta=2.0$, r=0.7, $\omega=3.0$, $\alpha=0$

There are two general types of periodic motion, and subclasses of each, which have been predicted for these systems. The particular motion which appears is dependent upon the system parameters and the initial conditions. The two general

types will be designated Type I and Type II. A Type I motion is a periodic motion impacting one constraint only, once per period of the motion, and Type II being a symmetric periodic motion impacting both constraints. Other types of motion are possible, but have not been dealt with in the analysis of the system. The normal pendulum can undergo motions of Type II along with the linear motions which do not impact the constraints. The inverted pendulum can undergo either Type I or Type II motions.

Subharmonic motions are observed for this system, these are of Type I and Type II and also other periodic motions. This represents the system responding to a periodic input with an output having a period which is an integer multiple of the input period. Subharmonics provide one mechanism for the development of chaos in systems.

Bifurcations occur when the dynamics of the system, for a certain parameter value, is qualitatively different for nearby parameter values. For the impacting pendulum, bifurcations are the mechanism by which periodic motions appear, change stability, and undergo qualitative changes. For the present case, a bifurcation diagram may be thought of as a graph of the amplitude of steady-state motion vs. a parameter. There are different types of bifurcations, depending upon the resulting solution curves and their stability. The general bifurcation classifications help in describing the system and provide a qualitative measure of the system dynamics. There are a limited number of typical bifurcation types which can occur, even in very complex systems. This result is due to the fact that the dynamics, near local bifurcations, may be reduced to simpler models using the ideas of center manifolds (Carr [20]). Details of bifurcation theory may be found in Guckenheimer and Holmes [5].

In the system studied, three types of local bifurcations were analyzed. These were saddle-node bifurcations, period doubling bifurcations, and pitchfork bifurcations. Bifurcation diagrams for each type are given in Figures 4,5, and 6 respectively. In these diagrams the branches depicted represent some measure of the amplitude of a periodic motion. Stability of the branches is as indicated in the Figures.

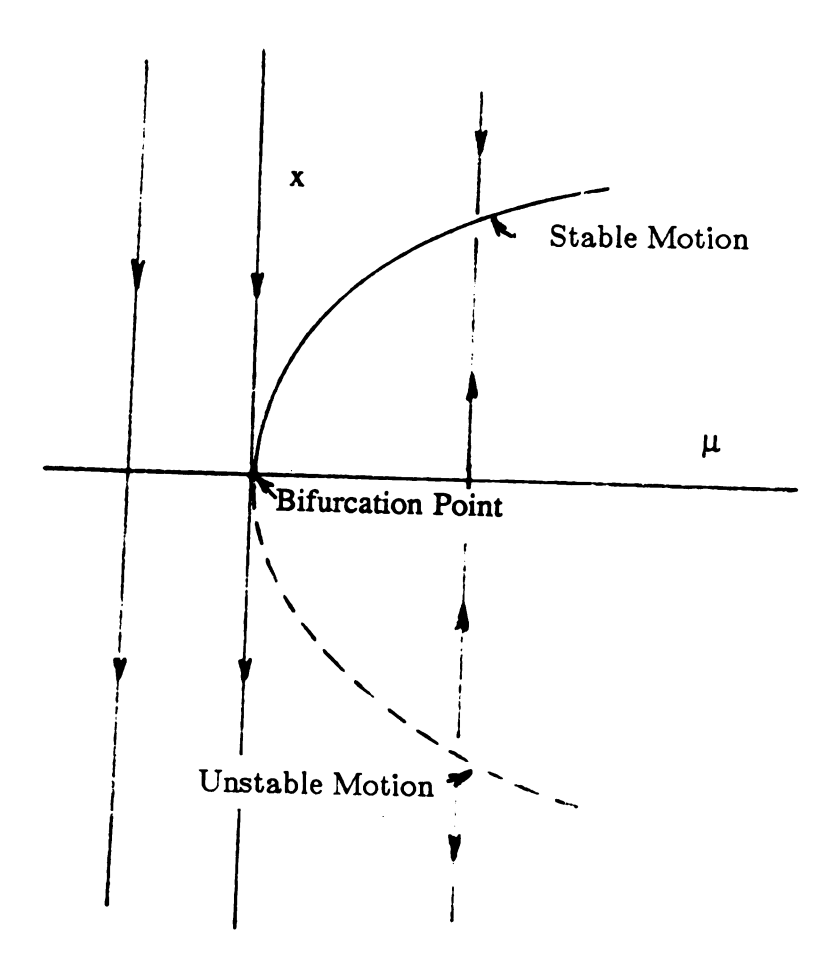


Figure 4 Saddle-node bifurcation

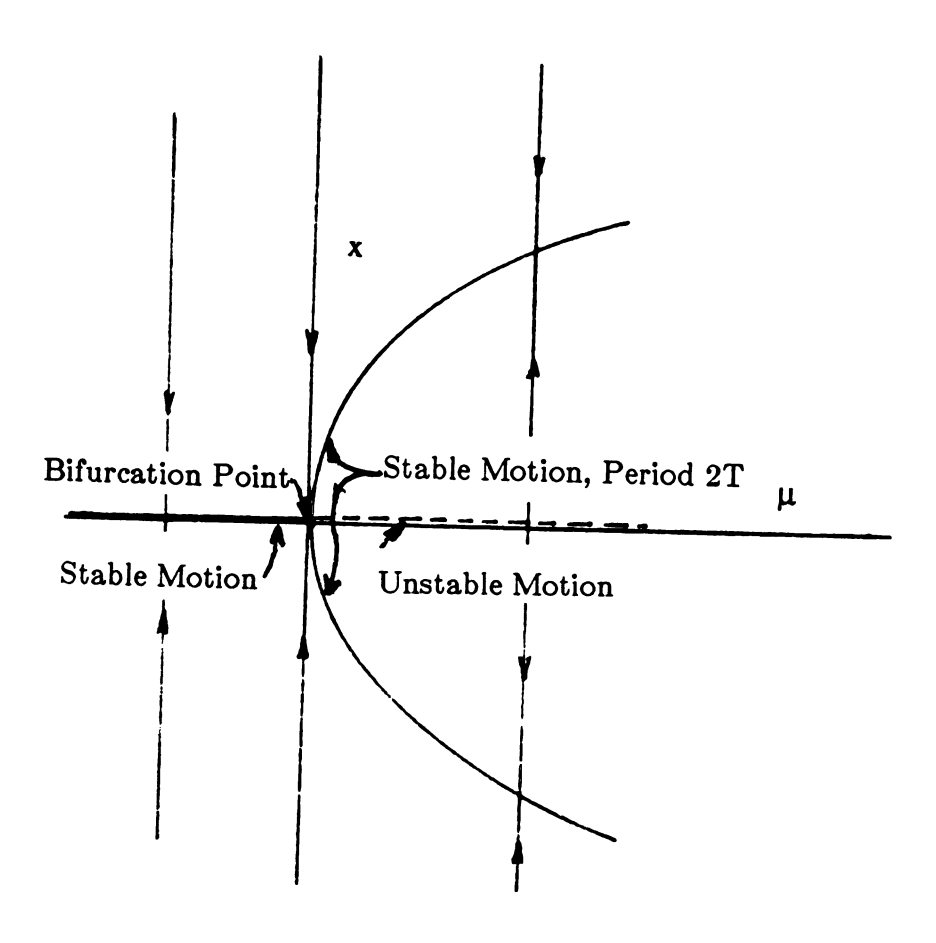


Figure 5 Period doubling bifurcation

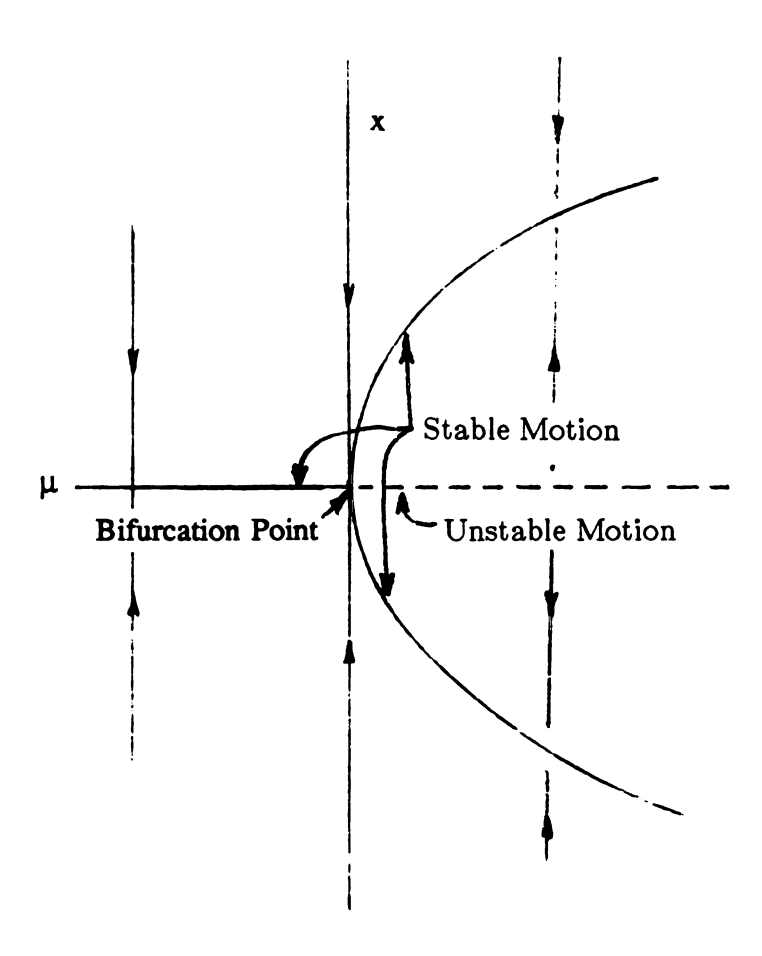


Figure 6 Pitchfork bifurcation

A saddle-node bifurcation occurs when a stable motion and an unstable motion converge and annihilate each other at the bifurcation point. Saddle-node bifurcations are a mechanism by which new steady-state motions can appear, where for nearby parameter regions, no periodic motions existed.

For this system, the saddle-node bifurcations for both Type I motions, impacting one constraint only, and Type II motions, impacting both constraints, are the first to occur as the driving amplitude is increased. An example of a Type I motions arising from saddle-node bifurcation is shown for the phase space of the inverted pendulum in Figure 7 (from digital simulation, see [1]). As a system parameter is varied, these periodic motions will exist and be stable until the next bifurcation point. Beyond that point, the motions will still exist, but will be unstable and therefore not experimentally observable. Typically, new stable motions will be born at the next, or secondary, bifurcation. Figure 8 shows a Type II motion in phase space for the inverted pendulum which arose from a saddle-node bifurcation (from [1]). Type II motions also arise from saddle-node bifurcations for the normal pendulum.

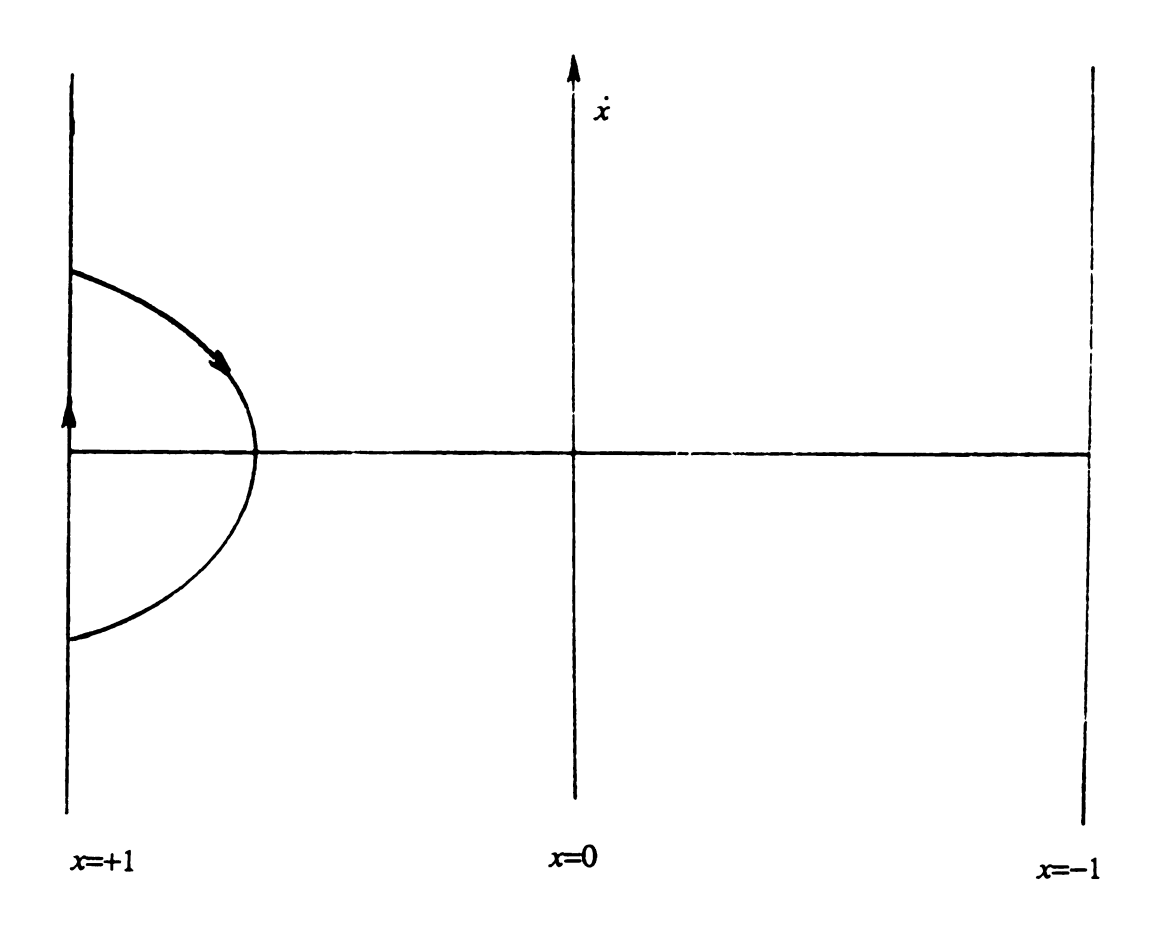


Figure 7 Motion from saddle-node bifurcation of Type I in phase space $\beta=0.6$, ~r=1.0 , $~\omega=4.0$, $~\alpha=0.1$

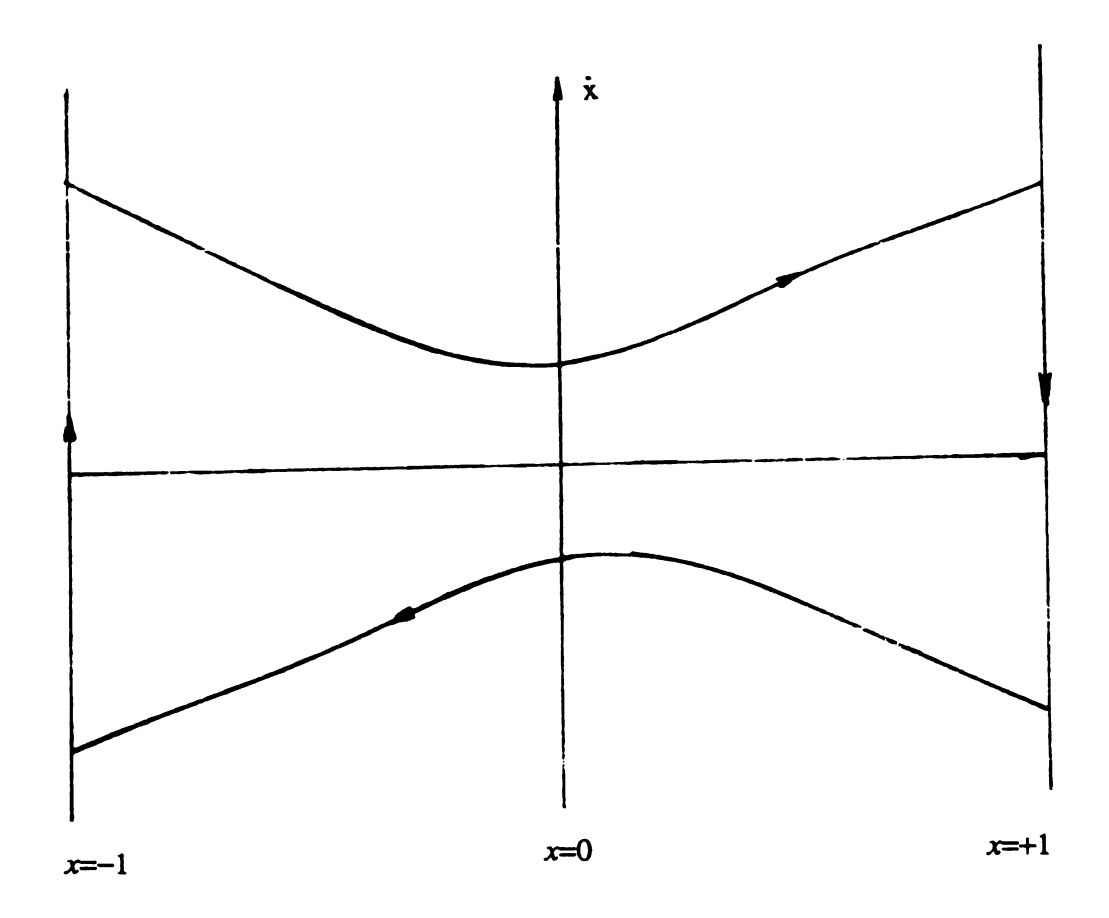


Figure 8 Motion from saddle-node bifurcation of Type II in phase space $\beta=2.3$, $\it r=1.0$, $\it \omega=1.95$, $\alpha=0.1$

A pitchfork bifurcation is the splitting of a branch, representing a symmetric solution, into two new stable branches with the old branch becoming unstable. This type of bifurcation is found in systems with symmetry as the two new stable motions are symmetrical about the old motion in the phase space. The new motion will have the same period as the original motion. Figure 9 shows the a motion arising from a pitchfork bifurcation in phase space for the inverted pendulum (from [1]). The pitchfork bifurcations are the secondary bifurcations of the Type II

motions. For parameter values just beyond the pitchfork bifurcation curves, these antisymmetric motions are expected to be observed.

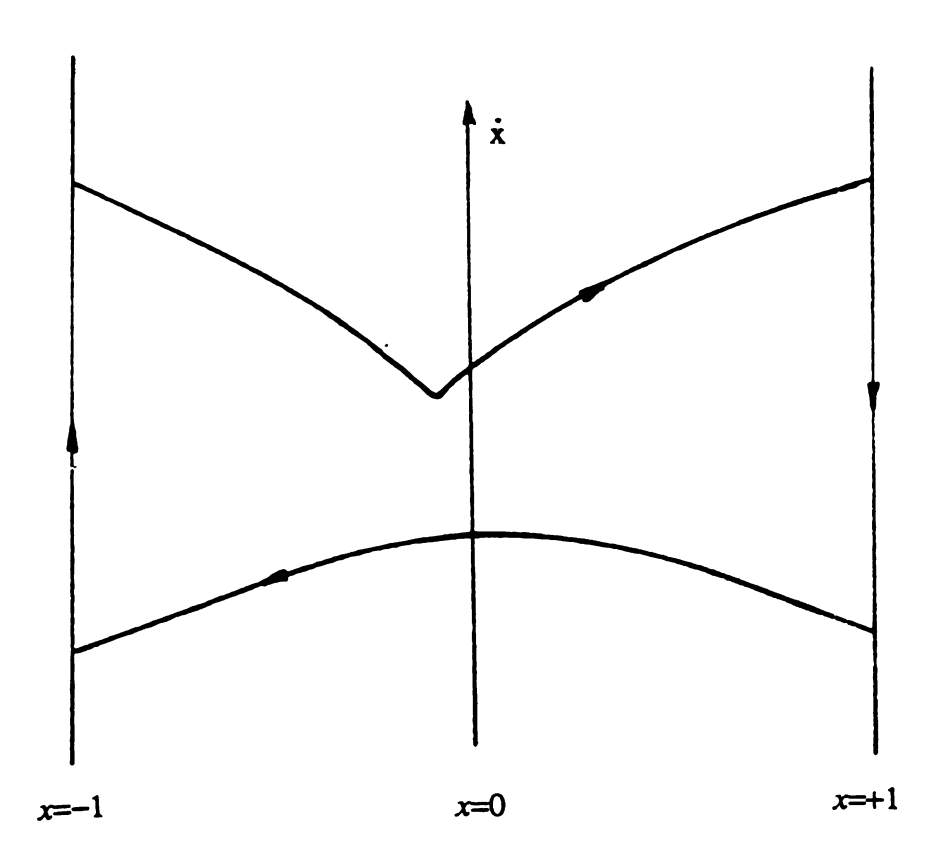


Figure 9 Motion from pitchfork bifurcation of Type II in phase space $\beta=2.3$, r=1.0 , $\omega=1.8$, $\alpha=0.1$

Period doubling bifurcations occur when a motion of period T becomes unstable and a new motion of period 2T is born. The bifurcation diagram is similar to the pitchfork diagram, the difference in being how the old stable motion loses stability. In the period doubling, the motion essentially 'flips', or alternates, between the two new stable branches, i.e., the two branches represent the *same* motion. An example of a period doubling motion in the phase space is given in Figure 10. Note that it repeats after two impacts while the original Type I motion

repeated after each impact. Period doublings occur in the inverted pendulum system when the stable Type I motions become unstable and the period doubled motions appeared. When period doubling bifurcations occur in rapid sequence, this is referred to as a period doubling cascade and is a precursor of chaotic motion in the system (Feigenbaum [21]).

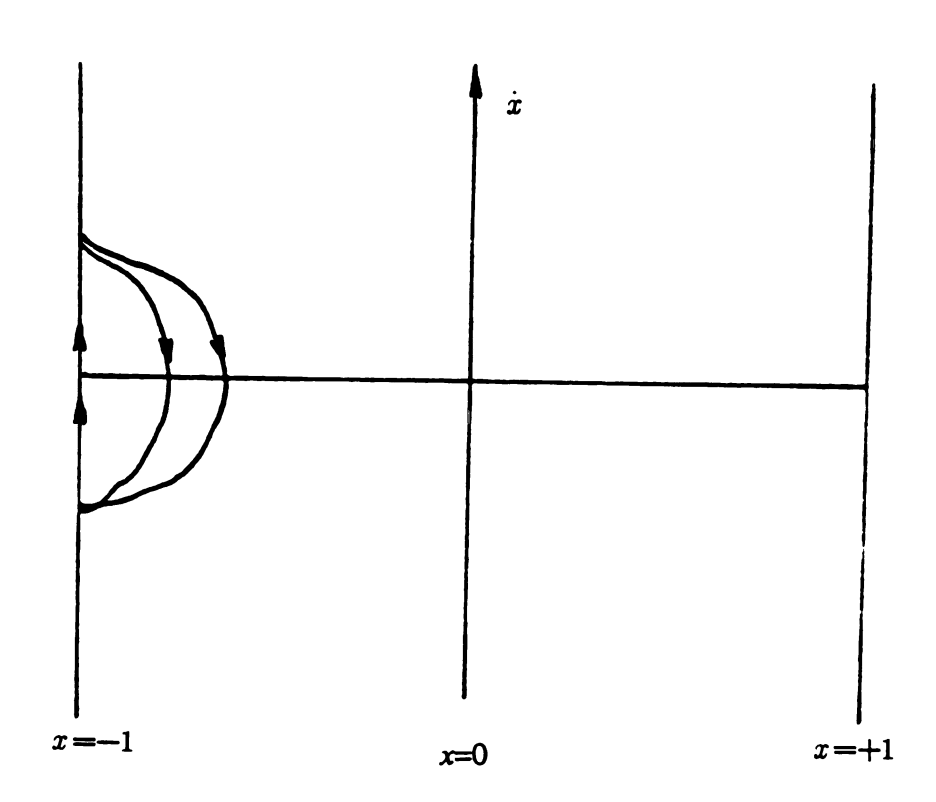


Figure 10 Motion from period doubling bifurcation of Type I in phase space

Chaotic motions are observed for this system, these arise in a global bifurcation as described in Shaw [1,3]. Chaos does not refer to randomness or disorder, but an unpredictable, complex, bounded, and deterministic motion of the system. Chaotic motion is not random in that there are no stochastic inputs or parameters. While chaos has broadband frequency content, the components will form patterns,

depending on the parameters of the system, with a few frequencies dominating. It comes about due to very complicated mixing and recirculation of trajectories in the phase space of the system (Guckenheimer and Holmes [5]).

The experimentally observed motions were ones which have a robust stability region in parameter space and in initial condition space, as they all appeared within one minute of the initial conditions and persisted for as long as the author cared to watch. To observe motions for which the corresponding stability windows are small, one would either need a precise choice for initial conditions and/or observation for a long time period. At many parameter values, there are a large number of stable solutions possible. The initial conditions to produce a certain motion are not known, we simply started the system and watched what developed. For some parameter values it is assumed that the initial condition boundaries which lead to the appearance of different motions is of a fractal nature [6] with a number of competing attractors. In such a case, extremely small changes in initial conditions will lead to drastically different steady state responses [5].

Noise, in the form of unmodeled inputs, exists in the physical experiment, as it does in any experiment or computer simulation (due to finite precision). In some parameter regions, periodic motions (typically those of large period) are predicted by the model which have extremely small stability windows in parameter space and the set of initial conditions which lead to that motion, i.e. the *domain of attraction*, is very small [5]. When the noise level is such that the resulting disturbances are larger than the domain of attraction of a given motion, then that motion will not be observed in the experiment. See [1,5] for further discussion of these issues. The conclusion of all of this is there are motions predicted by the model which will never be observed. These are typically those of very long period which, in any case, may be practically indistinguishable from chaos.

2. Experimental Equipment and Procedures

Design of the experimental apparatus was driven by the need to match, as closely as possible, the conditions of the analysis. These included a single degree of freedom system, i.e only the rigid body mode active; instantaneous, dissipative impacts at the constraints; linear viscous damping in the bearing; and a sinusoidal displacement of the support. The design selected has been used and improved to the current state from several months of experimental observations.

The dimensions of the experimental apparatus are as follows. The distance between the constraints, $2l\theta_{\rm max}$, is 6.6 cm. The length of the pendulum l is 25.3 cm. The mass of the pendulum m is approximately 0.05 kg. The exact value of the mass is not important as it does not appear in any of the nondimensional quantities except the damping ratio and the damping ratio was measured experimentally. The natural frequency of the system is 0.98 Hz. This gives the nondimensionalizing parameter between the natural frequency of the system $\sqrt{g/l}$, and the nondimensional driving frequency, $\omega = \omega_{dr}/0.98$. The β nondimensional calibration value was 26.0 mV/ β . This came from an accelerometer calibration of 201.6 mV/g and the geometry of the system. Details on the accelerometer calibration are given later.

Determination of the two system parameters, α and r, which remained fixed throughout the experiment, was done as follows. The coefficient of restitution, r, was assumed to be constant. We analyzed the time derivative of the angular displacement signal when impacts were occurring by using the differentiation hardware built in the Hewlett-Packard 5423A structural dynamics analyzer. The coefficient of restitution was assumed to be the ratio of the velocity after impact to

the velocity before impact. The value computed was $r=0.95\pm0.04$. The uncertainty is caused primarily by the coefficient of restitution having a dependence on the velocity at impact. We have assumed only a linear relation between impact velocity and rebound velocity. The damping coefficient α was obtained by hanging the pendulum in the normal position, giving the system an initial condition such that is did not contact the constraints, and recording the subsequent motion of the pendulum. A logarithmic decrement method was used on the data obtained to determine the damping value. The damping for this system was determined to be 0.03. A value for the uncertainty of the α value is not known, but since the results only depend on α to the first order, a 100% error in the damping value, or ±0.03 , will only result in a 3% change in the predicted bifurcation curves. The dissipation exhibited Coulomb damping components, so this value is an equivalent damping value. Both the damping ratio and the coefficient of restitution are dimensionless constants.

Keeping higher order modal vibrations out of the system was judged to be the critical design condition as these are easily excited at impacts. Other parameters were allowed slight variations from ideal, but the assumption of single degree of freedom had to be preserved as closely as possible if the experiment was to maintain the validity of the analysis. Excitation of higher modes at impact is inevitable, the effects of this can be minimized by a choice of a bar with a high flexural stiffness and relatively large structural damping. This will keep flexural displacements small and will damp out these higher modes quickly. To this end, a tube of graphite composite material was selected for the rod. Mathematical analysis of the impact process, along with experimental observation of impacts, showed the rod to have insignificant energy in the higher order modes for this system (Appendix A). Also, the energy which was transferred to these higher modes could

be thought of as being lost at impact, and lumped in with the coefficient of restitution. This assumption is reasonable since most of the transient higher mode vibrations, excited at impact, would decay before the next impact. The high stiffness to weight ratio of the graphite composite, along with the structural damping inherent in the material, proved to approximate the rigid, massless beam quite well for our purposes.

Once the pendulum beam was chosen, a mass was needed for the end. The qualities desired here were the ability to provide for nearly instantaneous impacts, but to minimize excitation the higher modes of the beam. For these reasons, a hard rubber ball was chosen as the pendulum mass.

The other design considerations were linear viscous damping in the bearing and a rigid structure to house the system and provide the constraints. Standard ball bearings were chosen to keep the damping low and as close to viscous as possible. The low damping and approximate viscous behavior come from the fact that the bearings provide a rolling friction environment as opposed to a sliding friction one. The bearings were mounted in two pillow blocks to provide uniform support for the pendulum. The frame was constructed out of 5mm aluminum T stock. This provided both the rigidity needed for the constraints and kept the weight low. This low weight allowed an electrodynamic shaker to be used as the driving device. With this shaker, both large forces and clean sinusoidal signals could be applied to the frame without significant feedback from the motion and impacts of the pendulum. At an excitation frequency of 10 Hz, the highest harmonic observed in the shaker was -48 db at 20 Hz.

The sensing system for the impacting pendulum was built around a Hall effect sensor. A circular permanent magnet was attached to the end of the shaft running through the mounting bearings. The Hall effect sensor was attached to the frame near the magnet to pick up the variations in the magnetic field. The magnet was oriented such that the magnetic field could be approximated by a linear function of the output voltage. The signal provided from the sensor was therefore proportional to the angular displacement of the pendulum. Due to the small angles involved, this signal could be used as a linear signal of the pendulum mass position. A circuit was provided to zero the output of the sensor at 0 degrees displacement. The magnetic field from he electromagnetic shaker produced no noticeable change in output of the Hall effect sensor. The linearity of the sensor was checked by having the pendulum in the normal position and checking that zero volts DC was the output in the equilibrium position and ± K volts existed for the pendulum in contact with the $+\theta_{max}$ and the $-\theta_{max}$ conditions, respectively. Data was then gathered on the output voltage vs. the pendulum position. The relationship between pendulum position and sensor output voltage was found to approximate a linear function with a linear regression coefficient of 0.99. Further details and the calibration curve are in Appendix C.

An accelerometer was mounted to the base of the frame to provide information on the excitation input to the pendulum system. The accelerometer calibration of 201.6 mV/g from the manufacturer's specification sheet was checked against a reference accelerometer at 10 Hz, a representative frequency for this experiment. No measurable deviation from the manufacturer's calibration was observed in the amplitude response of the accelerometer.

These two signals, the displacement from the Hall effect sensor and the signal from the accelerometer, along with the excitation frequency, provided the information required to map out the motions in the parameter space of the system. The signals obtained from the sensors were input into a Hewlett-Packard 5423A

structural dynamics analyzer. The Hall effect sensor signal was observed as a time trace to determine the type of motion present in the system at the particular parameter values. The acceleration signal was analyzed in the frequency domain to determine the magnitude of the acceleration at the excitation frequency ω_{dr} . The acceleration is part of the nondimensional excitation parameter β . The acceleration signal was also analyzed to determine if any other harmonics of the forcing frequency were present. In no case were any harmonics greater than -20db of the excitation signal observed. These higher harmonics are due to the impacts of the pendulum with the constraints. Thus the impact harmonics dominate the harmonics which are observed in the experiment.

The experimental procedure was performed as follows:

- 1- Turn on shaker and set to standby. Turn on the signal generator, sensing electronics and the measuring electronics; wait five minutes for the equipment to warm up.
 - 2- Set signal generator to desired frequency. (sets ω)
 - 3- Activate shaker.
 - 4- Set shaker amplitude to appropriate level. (sets β)
 - 5- Measure acceleration of the system.
- 6- Observe and record type of motion present, save time trace to tape if hardcopy is desired.
- 7- Change initial conditions of system by providing a small impact to the pendulum mass. This allows for the observation of motions coexisting at the same

system parameter values β , ω . Repeat 6-7 several times.

- 8- Return to number 4 until all easily observable motions have been found (Easily observable means within 1-2 minutes).
- 9- Return to step 2 as often as desired. A parameter map will require at several different frequency values in the range under study to provide good resolution.
 - 10- Turn shaker amplifier off.
 - 11- Turn off all devices.

See Figure 11 for a schematic of the experiment. In the particular setup used for this experiment, a voltage sum and null circuit were provided to condition the signal from the Hall effect sensor. This allowed the spectral analyzer to be set an a mode where the analyzer could process the signal accurately. The unprocessed output from the Hall effect sensor was a voltage level between 0-15 volts DC. The spectral analyzer performed better when the signals were a balanced \pm voltage level. Therefore, a negative voltage was applied and summed with the signal voltage to produce an output having the same magnitude at the constraints and zero output at zero deflection angle of the pendulum.

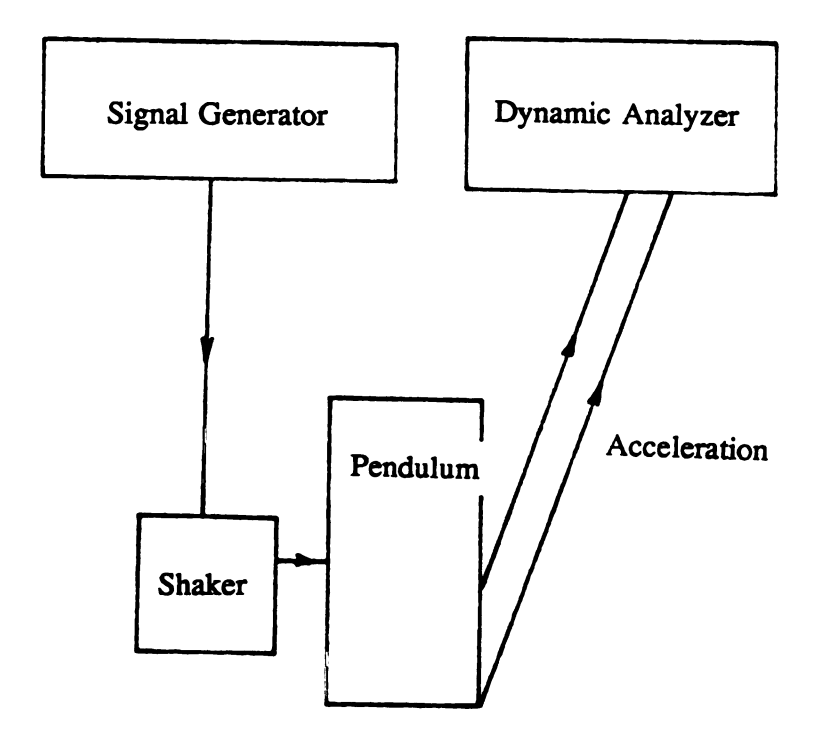


Figure 11 Experimental equipment

3. Results

3.1 Inverted Pendulum

The results of the experiments for the inverted pendulum are given in Figures 12 and 13. These figures show the observed motions vs. the predicted bifurcation curves from Shaw [1] in the β , ω parameter space for Type I and Type II motions of the inverted pendulum, respectively. The letters correspond to motions which exist at the point in parameter space given by the lower left corner of the first letter. The lines on the figures are the bifurcation curves, above which the associated motion exists. For Figure 12, the $\beta_n^I(SN)$ curves give the set of points above which we expect to find Type I periodic motions of period nT, impacting one wall only. The motions born at the the saddle-node bifurcations will exist and be stable until the corresponding $\beta_n^I(PD)$ curve is reached. At these parameter values, the Type I motion loses stability and a new motion of period 2T with two impacts is born. Therefore, in the region between the $\beta_n^I(SN)$ curves and the $\beta_n^I(PD)$ curves we expect to observe the Type I motion. Just above the $\beta_n^I(PD)$ curves, we expect to observe the associated period 2T motions.

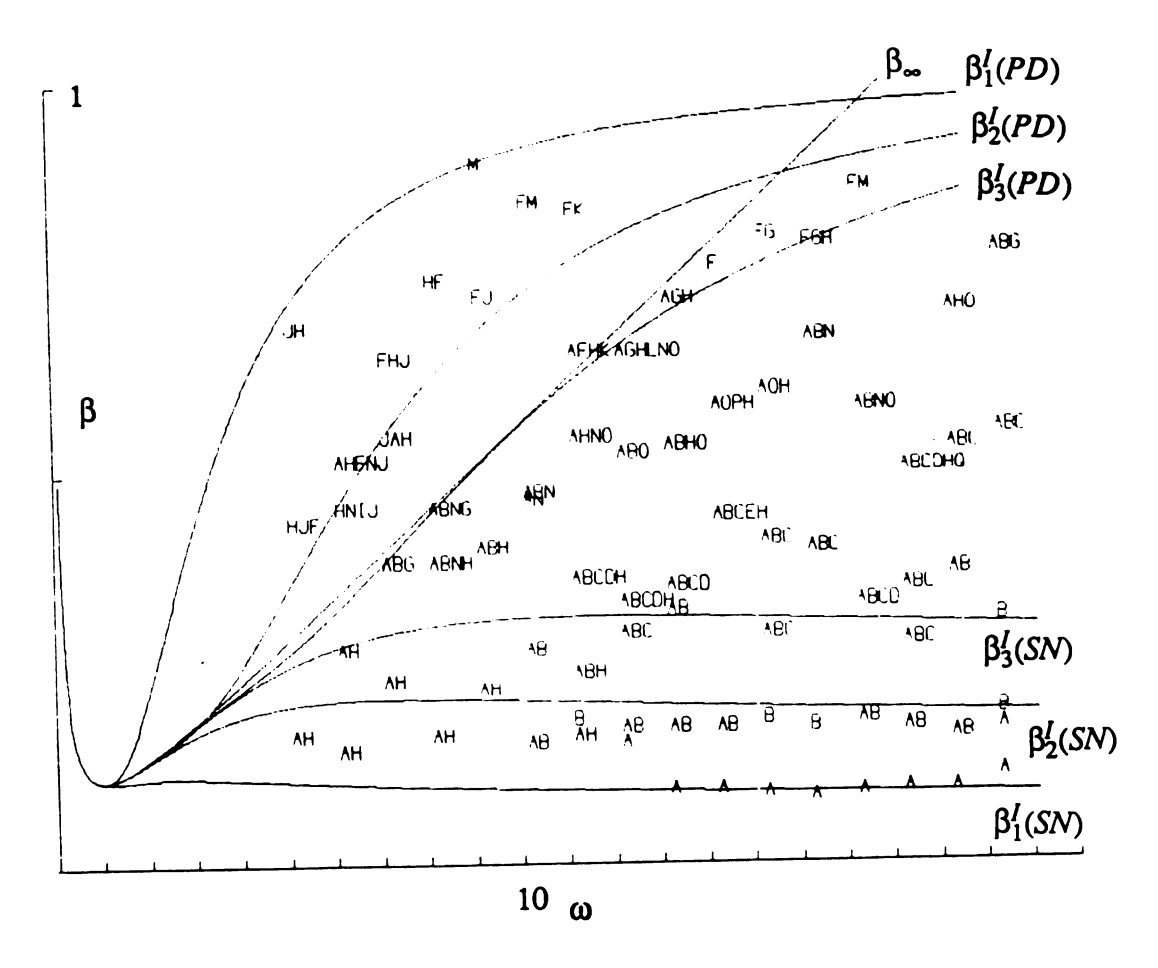


Figure 12 Experimental observations of Type I motions vs. predictions

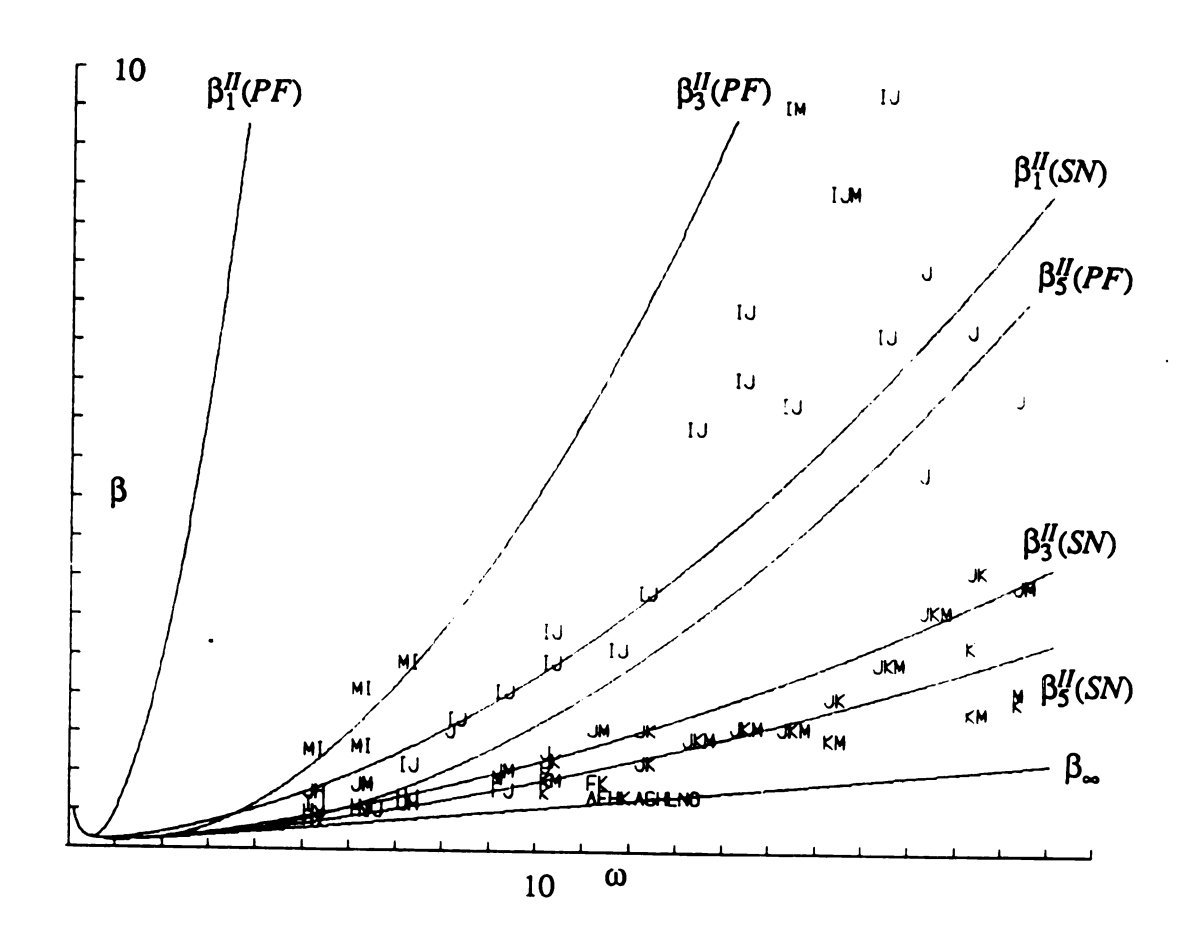


Figure 13 Experimental observations of Type II motions vs. predictions

Looking at Figure 12, we observe the motions corresponding to the $\beta_1^I(SN)$ are given by the letter A. Figure 14 shows an example of this motion in a time trace along with a representative excitation signal. That the signal is not perfectly periodic is due to the small amplitudes of the motion present. Therefore any noise or external vibration will show in the signal. The data was taken so as to show the lowest points for which the motion existed. For the higher frequencies, the agreement with the predicted bound is good. The $\beta_2^I(SN)$ curve gives the values above which we expect to see motions of letter B occur. Figure 15 gives a time trace of the motion corresponding to letter B along with the excitation signal. Again note the correspondence between the predicted values for the motion to exist and the actual experimental results. The $\beta_3^I(SN)$ curve gives the parameter values above which we expect motions corresponding to letter C to exist. Figure 16 shows the motion corresponding to C along with a representaive excitation signal. Note that the region above the $\beta_3^l(SN)$ curve but below the $\beta_3^l(PD)$ curve, A,B, and C motions exist and are stable. Figure 17 gives the motion corresponding to the letter D along with a representaive excitation signal. The letter E corresponds to Type I motion from a saddle-node bifurcation of period 5T with one impact per period.

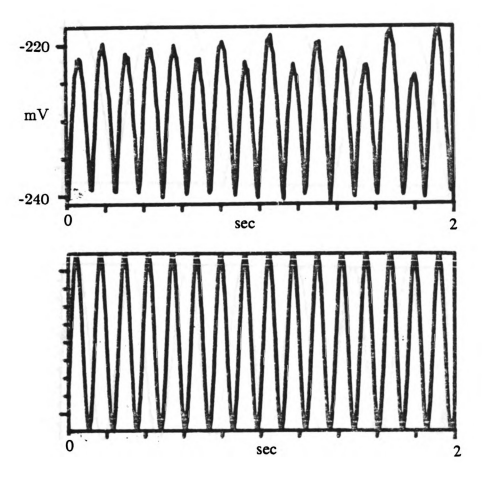


Figure 14 Type I motion from a saddle-node bifurcation, period T

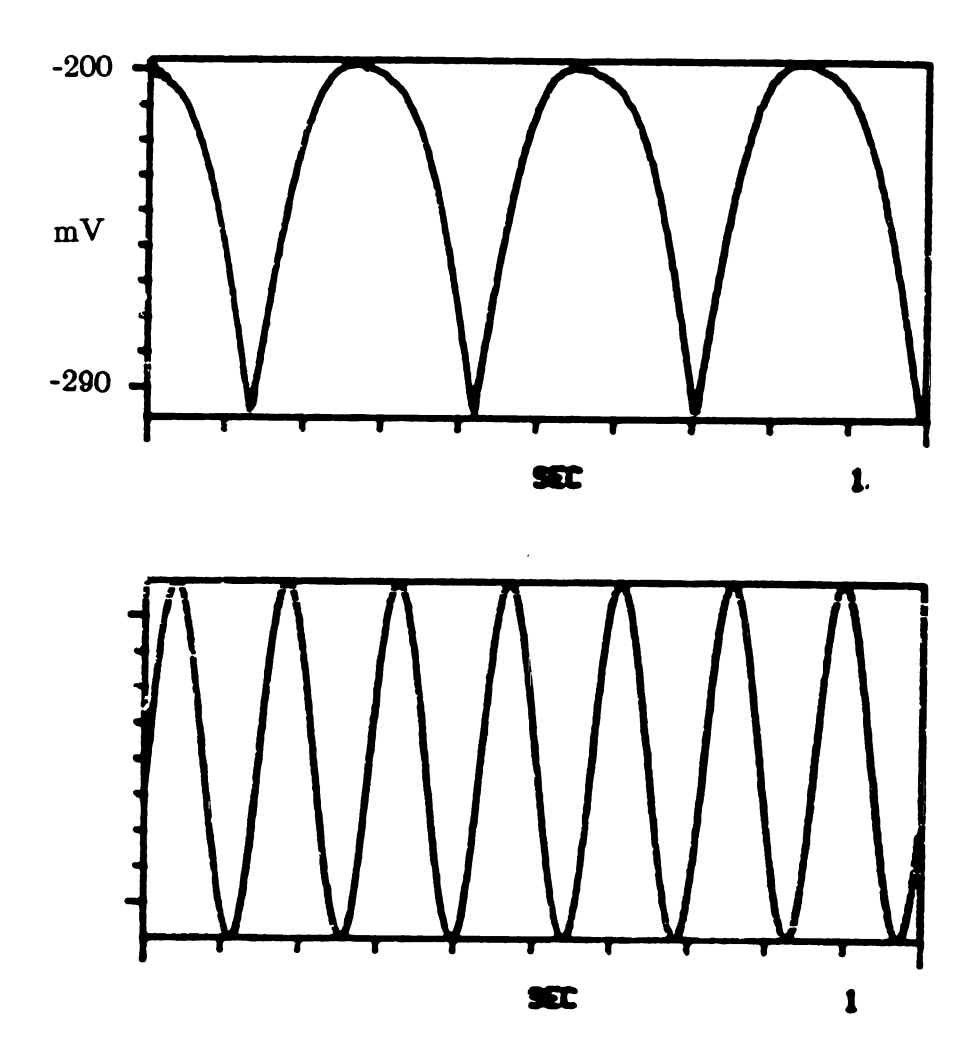


Figure 15 Type I motion from a saddle-node bifurcation, period 2T

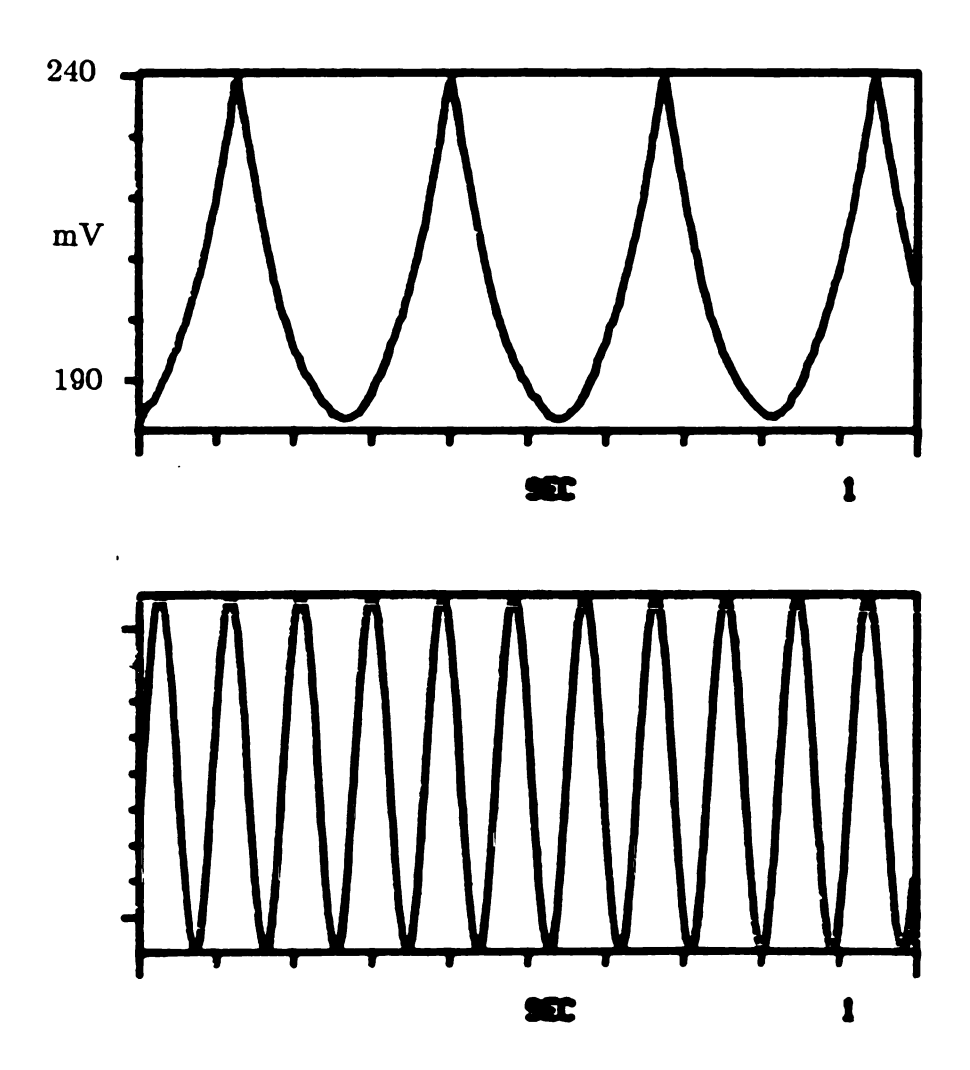


Figure 16 Type I motion from a saddle-node bifurcation, period 3T

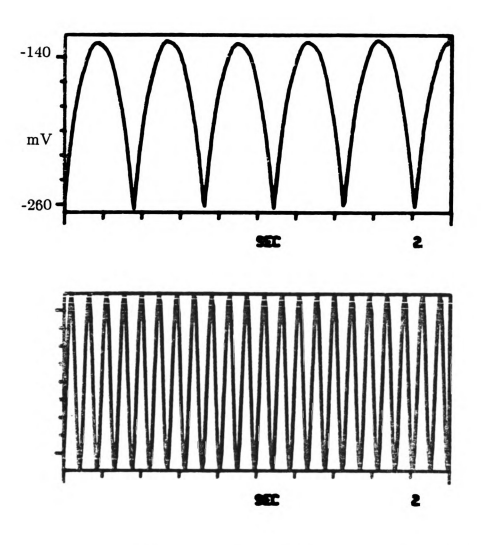


Figure 17 Type I motion from a saddle-node bifurcation, period 4T

The $\beta_1'(PD)$ curve gives the expected parameter values for which we expect the A motions to lose stability and motions corresponding to the letter F to arise. Figure 18 shows a time trace of the period doubling motion corresponding to letter F and a representative excitation signal. This signal is not perfectly periodic due to the same small amplitude and noise considerations as for Figure 14. The agreement between the experimental results and the predictions is not as good as for the $\beta_n'(SN)$ motions but the general trend does occur as expected. The motions corresponding to F and the next higher period doubling G, the motion shown in Figure 19 with a representative excitation signal, appear at lower β values than predicted.

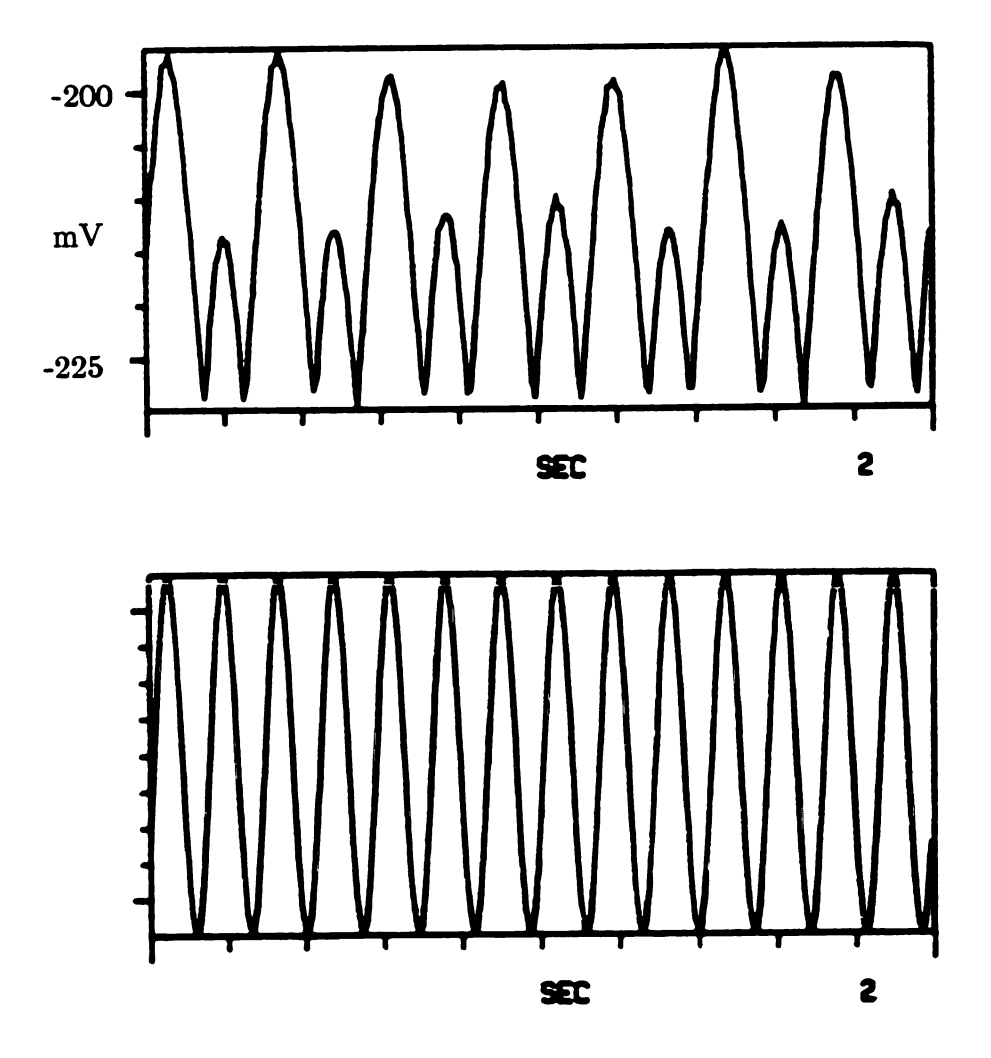


Figure 18 Type I motion from a period doubling bifurcation, period 2T

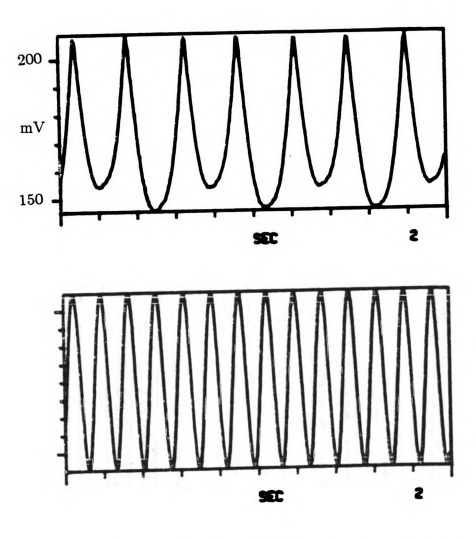


Figure 19 Type I motion from a period doubling bifurcation, period 4T

The curve denoted β_{∞} gives the limit curve as $n \to \infty$ for all the bifurcation curves. This means that all the curves will accumulate onto this curve as n approaces infinity. Therefore, above this curve, an infinity of unstable periodic motions exist. This curve is the parameter conditions above which chaos may occur. Choatic motions are represented by the letter M and a time trace of chaos is shown in Figure 20. Notice however, that an infinity of stable motions also exist above this curve so chaos may not appear as the 'steady-state' motion.

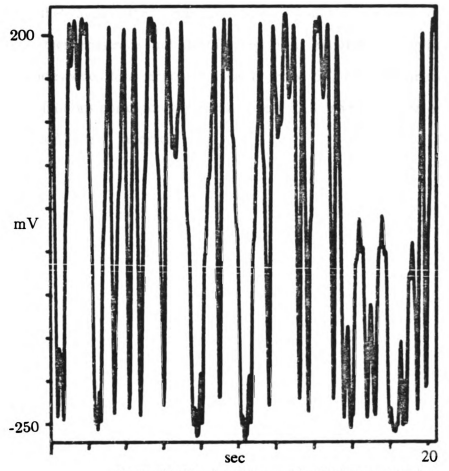


Figure 20 Chaotic motion, angular displacement vs. time

For all parameter values above the $\beta_1'(SN)$ curve, at least two motions, or solutions to the differential equation with the parameters $\beta_1\omega$, exist. One of these motions may be the rest case, the motion where the mass stays in contact with one

of the constraints and denoted by the letter H, see Appendix B. The existence of more than one stable steady-state motion means that the one which occurs depends upon the initial conditions given to the system. This is how both chaos and a stable periodic motion can coexist for the same parameter values.

The other periodic motions given by the letters N,O and Q are shown in a time trace with a representative excitation signal in Figures 21-23, respectively. No predictions on the regions of existence and stability of these motions exist. It was expected that these other periodic motions would occur, but the analysis to determine their existence and stability regions is extremely complicated [1]. The letter P corresponds to a motion of Type I, period 6T, with two impacts per period. The other motions corresponding to the letters I,J,K, and L will be discussed in the discussion of Type II motions.

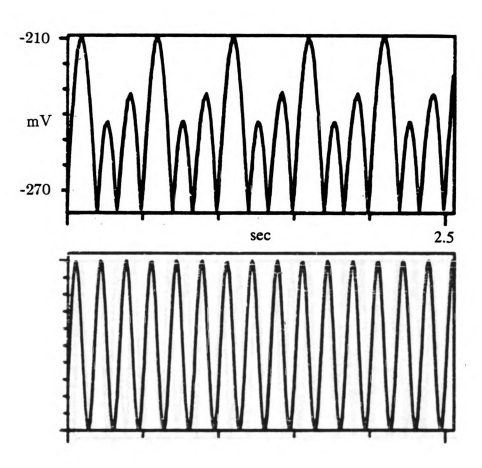


Figure 21 Other periodic motion, inverted pendulum, period 3, 3 impacts per period

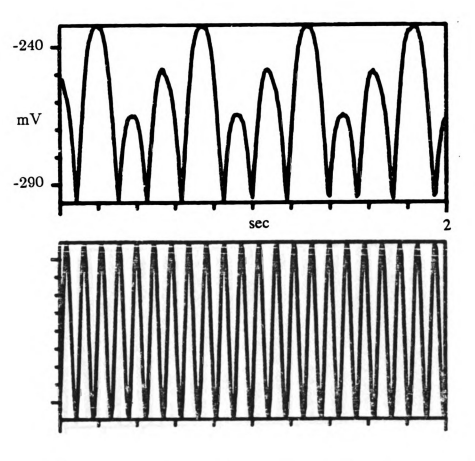


Figure 22 Other periodic motion, inverted pendulum, period 6, 3 impacts per period

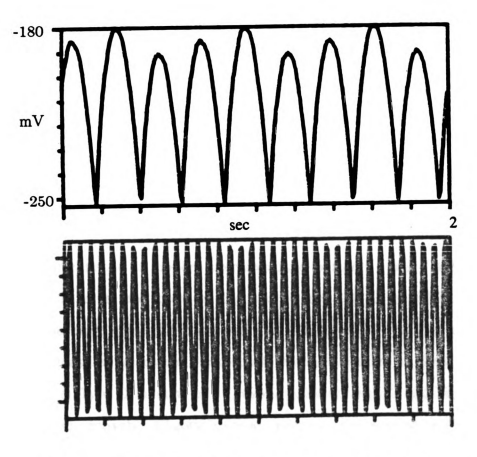


Figure 23 Other periodic motion, inverted pendulum, period 12, 3 impacts per period

Figure 13 shows the Type II experimentally observed motions vs. their associated bifurcation curves. Notice the difference in the β scale on Figure 13 as opposed to the β scale on Figure 12. This means that the Type II motions occur at larger excitation values than the Type I motions. This is intuitively correct as a larger excitation is required to push the inverted pendulum over the 'energy hill' of the unstable unforced equilibrium position and to the other side. Note that again, as for the Type I motions, there are $\beta_n^{II}(SN)$ bifurcation curves and associated $\beta_n^{II}(PF)$ bifurcation curves. For parameter values above the Type II saddle-node bifurcation curves, the associated motions exist and are stable until the corresponding pitchfork bifurcation curve is reached. At these points, the motions from the saddle-node bifurcations become unstable and two new antisymmetric periodic motions are born. Here the secondary bifurcation is a pitchfork rather than a period doubling due to the symmetry of the motion.

The time traces of motions corresponding to letters I and J are given along with representative excitation in Figures 24 and 25, respectively. While not showing the close correspondence with the saddle-node bifurcation curves as the Type I motions, the trends are as expected. Motions denoted by the letters K and L correspond to Type II motions of 5T, two impacts per period, and 7T, two impacts per period, respectively. Chaotic motions, given by the letter M, as for Figure 12, occured throughout the region above the β_{∞} curve and only a few were plotted for representation. No clear examples of motions arising from the secondary pitchfork bifurcations were observed. This may be due to two things. One is that the parameter region for some pitchfork motions to exist is for a large excitation (β) and low frequency (ω). Our experimenal apparatus was not able to provide excitation of this type. The second reason is that in a time trace of the motions, the motions from the saddle-node bifurcation and the motions from the pitchfork

bifurcation are very similar. A phase potrait of the motions is usually required to determine if the motion has undergone a pitchfork bifurcation. Thefore, some motions may have been from a pitchfork bifurcation, but were not able to be classified as such.

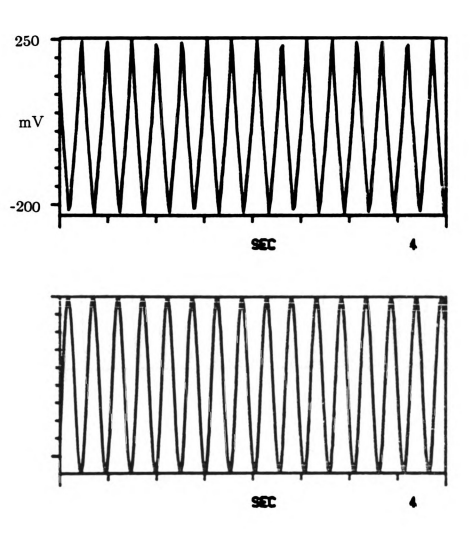


Figure 24 Type II motion from a saddle-node bifurcation, period T

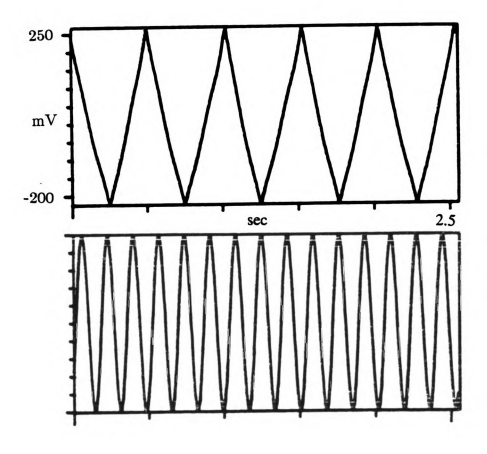


Figure 25 Type II motion from a saddle-node bifurcation, period 3T

On both Figures 12 and 13, there are parameter values for which both Type I and Type II motions coexisted. This was as expected, as for low ω values, there are regions where stable Type I and Type II motions coexist. Both figures show the general trends predicted in Shaw [1] for the response of the inverted pendulum system.

3.2 Normal Pendulum

Figure 26 shows the observed motions vs. the predicted bifurcation curves from Shaw [2] for the normal pendulum system. These bifurcation curves are for the case of no damping $(\alpha = 0)$. The assumption of no damping is reasonable due to the low value for the actual damping and the fact that the bifurcation curves depend on the damping only to the first order. Here we have linear motions and nonlinear motions coexisting. Linear motions are those which do not impact the constraints and the nonlinear motions are Type II, impacting both constraints. The $\beta_1(SN)$ curve are the parameter values above which the motions corresponding to the letter X are predicted to occur. This motion is of period T with two impacts per period. The $\beta_3(SN)$ curve gives the parameter values above which the motions given by the letter Y are expected to exist. Figure 27 gives a time trace of this motion along with a representative excitation signal. The $\beta_5(SN)$ curve gives the parameter values above which we expect to find the motions corresponding to letter Z. This motion is of period 5T with two impacts per period. No bifurcation curve for the $\beta_7(SN)$ was plotted, however motions arising from this bifurcation are denoted by the letter W.

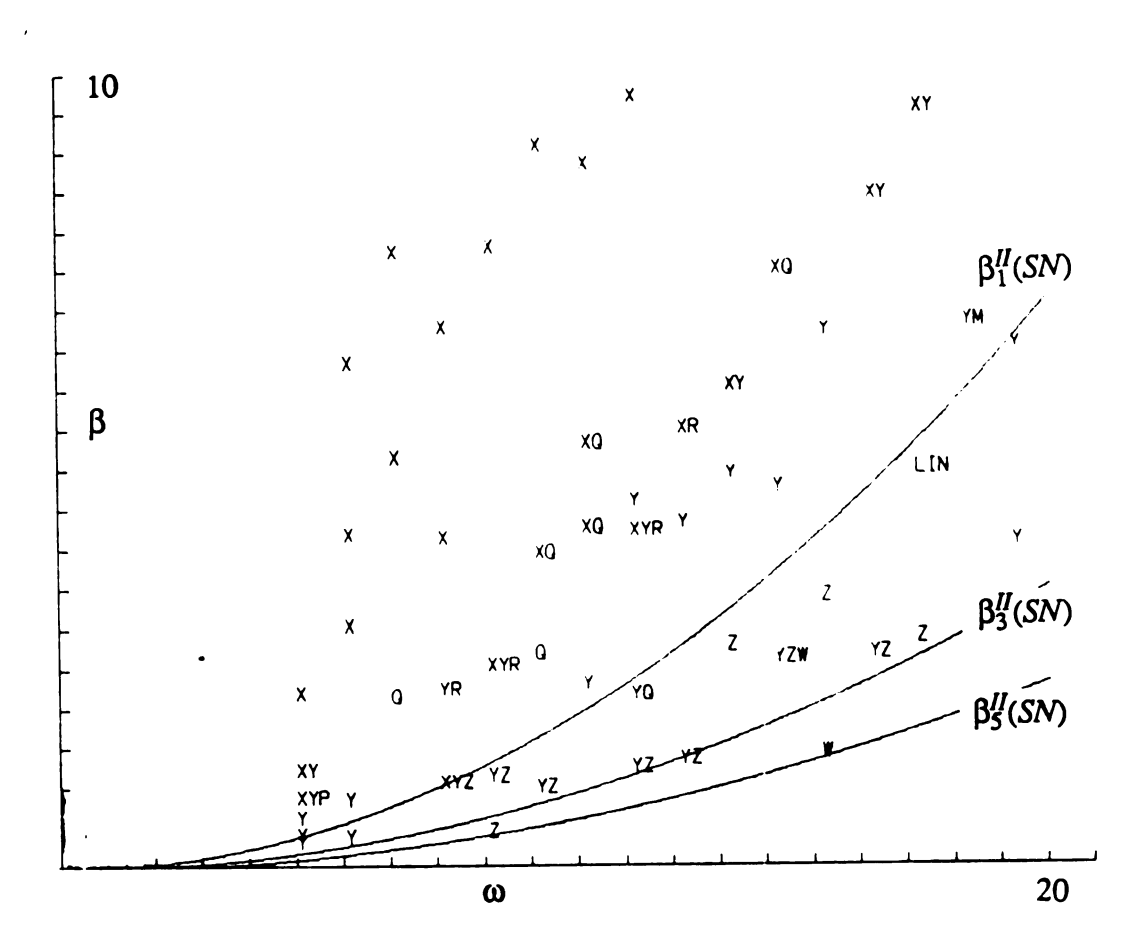


Figure 26 Experimental observations vs. predictions for normal pendulum

Key of Motions (Type, Period, Impacts per Period)	
X - II,1,2 Y - II,3,2 Z - II,5,2 W - II,7,2 Q - II,3,2,PF	R - II,9,6 P - II,6,2 M - Chaos LIN - Linear Motion Only

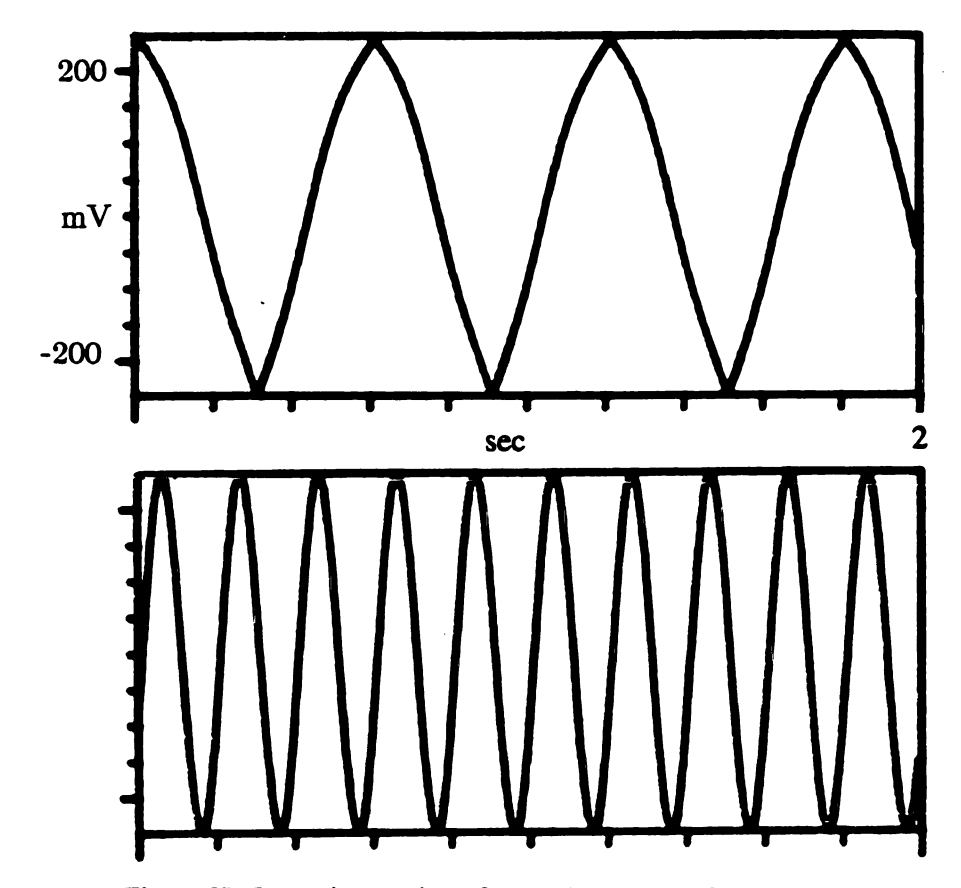


Figure 27 Impacting motion of normal pendulum from a saddle-node bifurcation, period 3T

In the normal pendulum system, the secondary bifurcations are of a pitchfork type as for the Type II motions in the inverted pendulum system. For the normal pendulum system, the difference between the motions from the saddle-node bifurcations and the motions from the pitchfork bifurcations were clearer than for the inverted pendulum system and some motions were able to be classified as arising from pitchfork bifurcations. The motions from the pitchfork bifurcation are given by letter Q. A time trace of this motion and a representative excitation signal are shown in Figure 28. The conditions for the pitchfork bifurcation to occur are not given explicitly by Shaw [2] and are hence not plotted in Figure 28. It is

expected that similar behavior occurs for the normal pendulum system as for the inverted pendulum system. This means that it is expected that there will be some region for which the motion from the saddle-node bifurcation will exist and be stable and a secondary bifurcation will occur where the motion from the saddle-node will lose stability and new motions will be born.

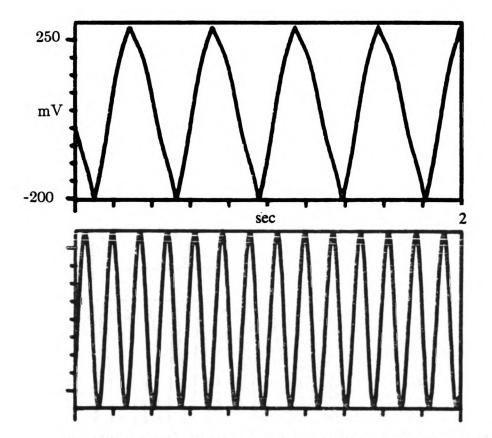


Figure 28 Impacting motion of normal pendulum from a pitchfork bifurcation, period 3T,

The motion denoted by the letter R represented another periodic impacting motion which was not able to be classified as from either a saddle-node bifurcation or a pitchfork bifurcation. A time trace and associated excitation signal for motion R is given in Figure 29. The letter P corresponds to a periodic motion of period 6T, with two impacts per period. The letter M, as for the inverted pendulum

system, corresponds to the observance of chaotic motions of the normal pendulum. For the normal pendulum, the occurance of chaos was not as widespread as for the inverted pendulum. The letters LIN denote a parameter value where only the linear, nonimpacting motion occured. Linear motions are not otherwise represented as they occurred everywhere throughout the parameter space.

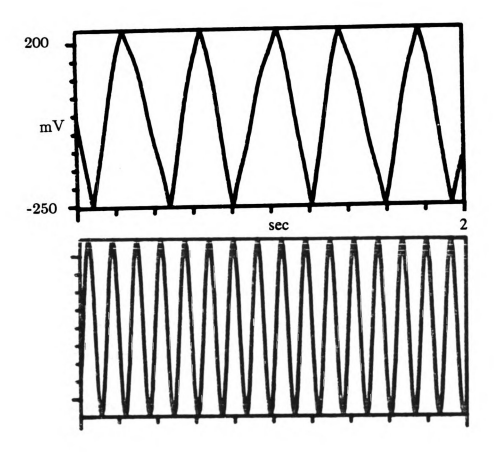


Figure 29 Other periodic motion, normal pendulum, period 9, 6 impacts per period

4. Discussion

This experiment validated the theoretical models used for normal and inverted pendulum systems. Observed motions closely corresponded to the predicted values. The small discrepancies from the predicted values were most likely from the assumptions made in the models of the systems. The assumptions of linear viscous friction in the bearing, single degree of freedom, and instantaneous impacts based on an impact rule proportional to velocity are all valid approximations this system but are not full descriptions of the reality of the situation. There was also experimental uncertainty in measuring the damping and the coefficient of restitution. Even with the errors in these assumptions, the system retained most of the predicted behavior.

The overall objective of this work was to confirm, in qualitative terms, the predictions of Shaw [1-3] and Sharif-Bahktiar and Shaw [16]. This thesis has demonstrated that the types of motions predicted do in fact occur and they occur in the regions of parameter space perdicted by the model. This experiment was designed more to prove the ideas in the model than to measure precise details of the motions. It was enough to know what type of motion was occuring and a reasonable measure of the parameters at which it occured.

On the question of improved equipment, one which would extend and benefit the experiment significantly would be a data acquisition system capable of long time record data at useful sampling frequencies. This would allow the generation of Poincare maps for the system. Along with the data acquisition equipment, software to automatically analyze the data would be convenient. Outlines and some details of this software have been completed but further work is required. Other equipment details involve high stability amplifiers for the sensing electronics and as much shielding of cables as possible to cut down on interference. Also, a real time analog differentiator with no phase lag would be useful for obtaining velocity signals.

This is one of the few works combining a theoretical, numerical, and experimental study of the same system. We have taken predictions from an analytic model and verified them, providing a good indication of the validity of the theoretical model. Having a theoretical knowledge of the system allowed for an experiment to be designed to test for specific results. Experimental evidence of chaos has been shown before [17-20], but typically is checked only against simulations or asymptotic analytic work. Due to the piecewise linear nature of the impacting pendulum, we were able to compare results from *exact* analysis [1,2,3,16], to simulations [1,2,3] and experiments [this thesis]. In fact, this was done for a wide range of motions from linear, nonimpacting motions, to various types of subharmonics as well as chaos. That the predictions and experiment agree so closely is a clear fact on the usefulness of bifurcation theory in engineering analysis.



Appendix A

Effect of Higher Modes of Vibration on the System

The dynamics of the pendulum system during and immediately following impacts will affect the subsequent motion of the pendulum. If modes other than the rigid body mode are present at subsequent impacts discrepancies will arise between the physical system and our simple model. Presented here are an analysis and simulation to verify our assumption of a single degree of freedom system. The analysis dealt with duration of impacts, the beam velocity profile at impact, and the velocity profile at release. This information will allow for determination of how much energy is transferred from the rigid body mode into higher modes at impact.

A uniform beam without the end mass is considered here. This is valid since during contact the mass remains fixed at the wall and plays no essential role in the flexing of the beam at impact. It will affect the dynamics of the beam after impact but not the amount of energy transferred to the higher modes during impact.

The analysis for the system switches back and forth between pinned-free and pinned-pinned modes depending on whether the system is in contact with the constraint or in free flight.

Consider a continuous system described by the partial differential equation (Meirovitch [22])

$$L\left[W(P,t)\right] + M(P) \frac{\partial^2 W(P,t)}{\partial t^2} = f(P,t) + F_j(t)\delta(P - P_j) . \tag{A.1}$$

This is the full equation of motion for a continuous beam with displacement and time varying applied forces. The L operator gives the fourth partial derivative with

respect to the solution W(P,t), M(P) is the mass distribution along the spatial variable P, the second partial gives the acceleration of the beam at that spatial location and time, the f(P,t) give the spatial and time varying forces on the beam, and $F_j(t)\delta(P-p_j)$ give the modal impulsive forces on the beam. The solution to equation A.1 may be expressed in a more familiar form as

$$W(P,t) = \sum_{r=1}^{\infty} w_r(P) \eta_r(t) + F_{all}$$
 (A.2)

This is the separation of variables for a continuous system with orthogonal eigenvectors.

The first section of analysis will determine the magnitude of the impulsive force needed to exactly stop the end (x(L)) of the beam. The velocity at the end of the beam will be zero at impact and the rest of the beam will have some velocity profile. The pinned-free mode shapes are given by

$$w_{r_{pl}}(x) = Cosh\left[\frac{\lambda_{i}x}{L}\right] - Cos\left[\frac{\lambda_{i}x}{L}\right] - \sigma_{i}\left[Sinh\left[\frac{\lambda_{i}x}{L}\right] - Sin\left[\frac{\lambda_{i}x}{L}\right]\right]$$
(A.3)

$$\sigma_i = \frac{\left[Cosh\lambda_i - Cos\lambda_i\right]}{Sinh\lambda_i - Sin\lambda_i} \tag{A.4}$$

The λ_i is given by the solution to the equation

$$Tan\lambda = Tanh\lambda$$
 (A.5)

The $w_r(x)$ are the mode shapes of the system and the $\eta_r(t)$ are the modal amplitudes, which are given by

$$\eta_r(t) = \frac{1}{\omega_r} \int_0^t N_r(\tau) \sin \omega_r(t-\tau) d\tau + \eta_r(0) \cos \omega_r t + \eta_r'(0) \frac{\sin \omega_r t}{\omega_r}$$
 (A.6)

$$\eta_r(0) = \int_D M(x) w_r(x) w(x,0) dx$$
(A.7)

$$\eta'_{r}(0) = \int_{D} M(x)w_{r}(x)w'(x,0)dx$$
 (A.8)

These equations correspond to the forces applied to the system, the initial displacement, and the initial velocity. For the system under consideration, the linear velocity is proportional to distance along the beam, Ωx , i.e. rigid rotation is assumed at an angular velocity Ω . The unknown impulsive force at x = L is \hat{F} . Substituting these values into the above equations yields

$$\eta_r(t) = \frac{1}{\omega_r} \int_0^t w_r(L) \hat{F} \delta(t) Sin\omega_r(t-\tau) d\tau + \int_0^L M(x) \ w_r(x) \Omega x \ dx \quad . \tag{A.9}$$

This reduces to

$$\eta_r(t) = \frac{w_r(l)\hat{F}}{\omega_r} \sin(w_r t) + \Omega M \int_0^l w_r(x)x \ dx \ . \tag{A.10}$$

This integral evaluates to

$$\left[\frac{L^2}{\lambda_i} - \frac{L^2}{\lambda_i^2}\right] Cosh\lambda_i + \left[\frac{L^2}{\lambda_i} - \frac{L^2}{\lambda_i^2}\right] Sinh\lambda_i
+ \left[\frac{L^2}{\lambda_i} - \frac{L^2}{\lambda_i^2}\right] Cos\lambda_i + \left[\frac{L^2}{\lambda_i} - \frac{L^2}{\lambda_i^2}\right] Sin\lambda_i$$
(A.11)

This equation will be expressed as $I(\lambda_i)$ in future calculations. Using this notation, the equation is

$$\eta_r(t) = \frac{w_r(L)\hat{F}}{\omega_r} Sin(\omega_r t) + I(\lambda_i) \frac{Sin(\omega_r t)}{\omega_r} . \tag{A.12}$$

Since $W(x,t) = w_r(x)\eta_r(t)$, the velocity at impact is given by the derivative with respect to time of the time function multiplied by the spatial function. The condition of zero velocity at end of the beam is $W'(L,0^+) = 0$, where $(') = \frac{\partial}{\partial t}$. The equation for \hat{F} is then

$$\hat{F}_r = \frac{-I(\lambda_i)\Omega M}{w_r(L)} \quad . \tag{A.13}$$

We now transfer to the pinned-pinned modes to evaluate how long the beam will remain in contact with the stop. To do so, the velocity profile from the pinned-free system just after impact will be used as initial conditions. The velocity profile is

$$W'_r(x,0) = w_r(x)_{pf} \left[(1 - \omega M)I(\lambda_i) \right] . \tag{A.14}$$

The pinned-pinned mode shapes are

$$W_r(x,t)_{pp} = Sin\left[\frac{i\pi x}{L}\right] \eta_r(t)_{pp} . \qquad (A.15)$$

$$\eta_r(t)_{pp} = \frac{Sin(\omega_r t)}{\omega_r} \int_0^L Sin\left[\frac{i\pi x}{L}\right] W'_r(x,0)_{pf} dx . \qquad (A.16)$$

The integral is a function of Sinh, Cosh, Sin, and Cos arguments. It may be broken into four separate integrals with the result as follows

$$II = M(1-M\Omega)\left[A + B - \sigma_i(C + D)\right]I(\lambda_i) . \tag{A.17}$$

A, B, C, and D are given as

$$A = \frac{Sin(p-q)L}{2(p-q)} - \frac{Cos(p+q)L}{2(p+q)}$$
 (A.17a)

$$B = \frac{-Cos(p-q)L}{2(p-q)} - \frac{Cos(p+q)L}{2(p+q)} + 2$$
 (A.17b)

$$C = \frac{aCosh(aL)Sin(pL) - pSinh(aL)Sin(pL)}{a^2 + p^2}$$
(A.17c)

$$D = \frac{aSinh(aL)Sin(pL) - pCosh(aL)Cos(aL)}{a^2 + p^2}$$
 (A.17d)

$$p = \frac{i\pi}{L} \qquad q = a = \frac{\lambda_i}{L} \tag{A.17e}$$

These equations for the initial conditions allow for the determination of the motion of the beam while it is contact with the constraint to be determined. The equation of motion is

$$W_i(x,t)_{pp} = Sin\left(\frac{i\pi x}{L}\right) II \frac{Sin(\omega_i t)}{\omega_i} . \tag{A.18}$$

The time the beam will remain in contact with the constraint is the time the shear force in the beam at x=L, V(L,t) is holding it against the wall. When V(L,t) becomes nonpositive, the beam will release from the wall since the stop cannot provide a force to maintain contact. The shear is the third spatial derivative of the displacement:

$$\frac{\partial^3 W_i(L,t)}{\partial x^3} = \frac{-i^2 \pi^2}{L^2} Cos(i\pi) II \frac{Sin(\omega_i t)}{\omega_i}$$
 (A.19)

Computer simulations were performed using these equations to determine the duration of impact and the amount of energy transmitted to higher modes. In Figure A1, the time required for the shear to change sign, and thus the impact time, is shown. Physical property values were investigated in the region of the values of the actual impacting system, and all simulations showed short impact times on the same order as Figure A1. The approximation of instantaneous impacts is therefore a reasonable one. The amount of energy input to each mode is represented by the magnitude of the \hat{F}_i 's. Simulations showed that less than $\frac{1}{2}$ of 1% of the impact energy was transmitted to higher modes for any impact velocity. Figure A2 shows the experimental time trace of multiple impacts as the pendulum velocity vs. time. After impact, there is a small amount of higher mode activity, but this is damped out by the structural damping in the system. The apparent persistent vibrations are

noise associated with 60 Hz electronic interference. The simulation and experimental evidence show the assumption of a single degree of freedom system to be valid for this experiment.

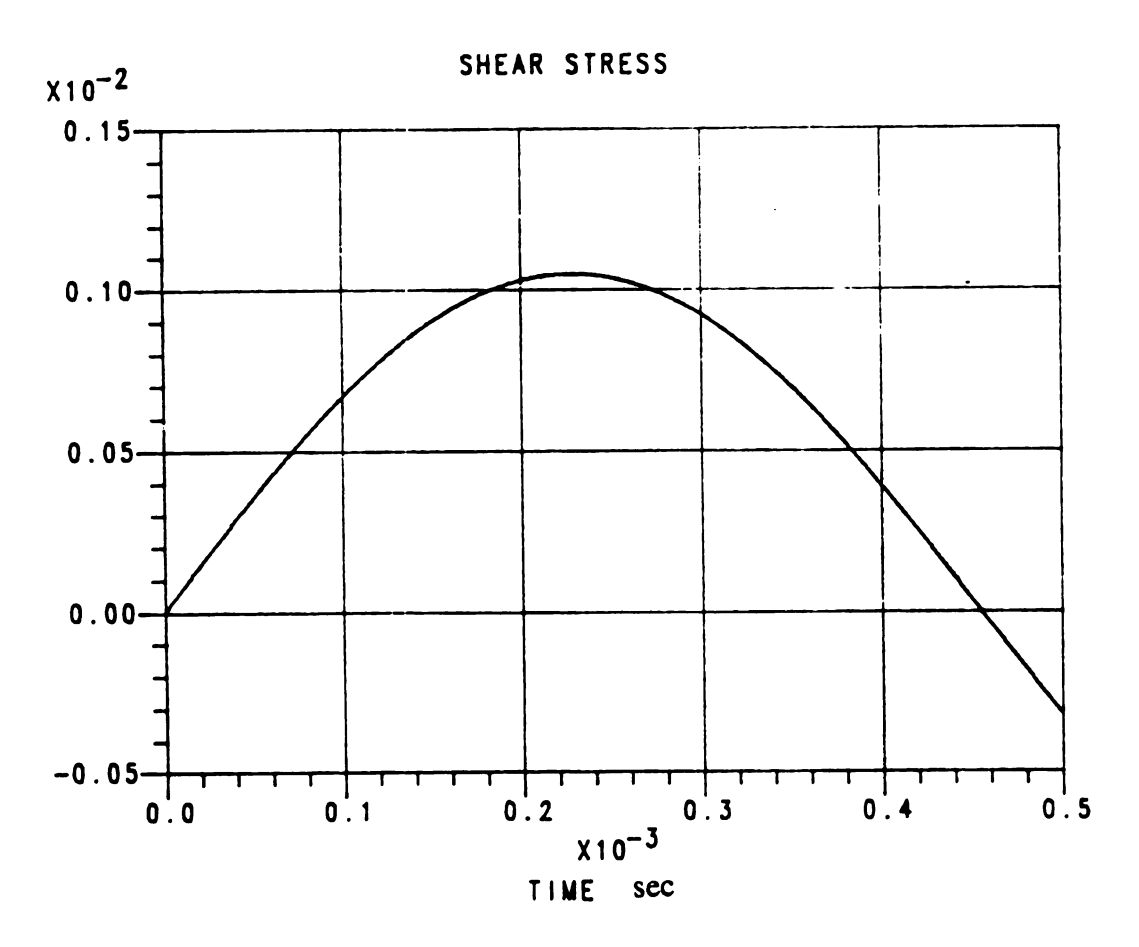


Figure A1 Simulation of shear at x=L

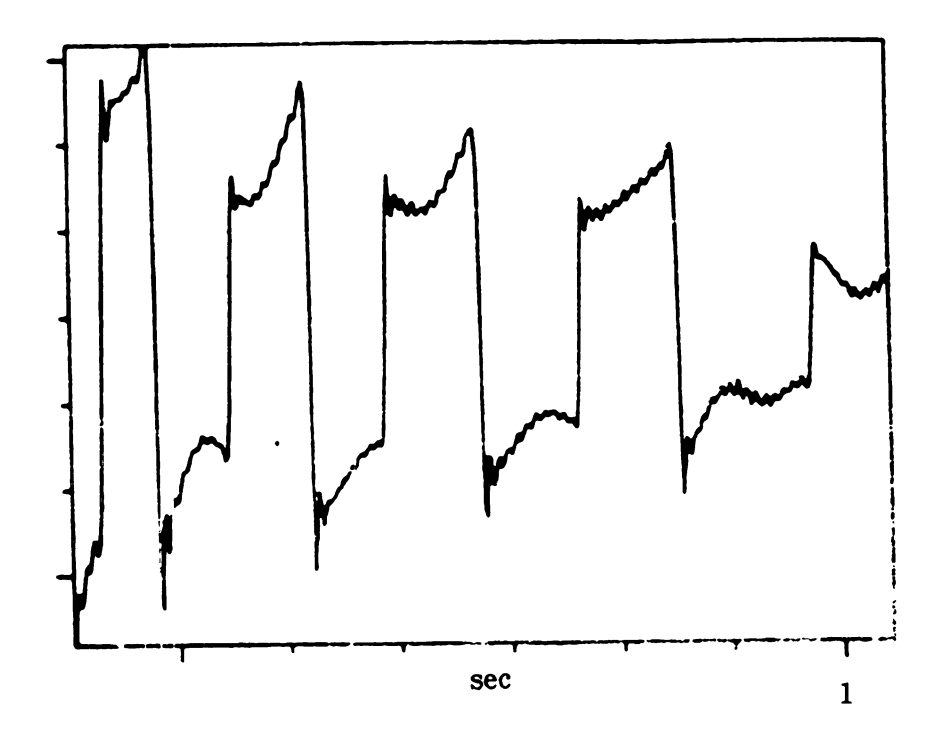
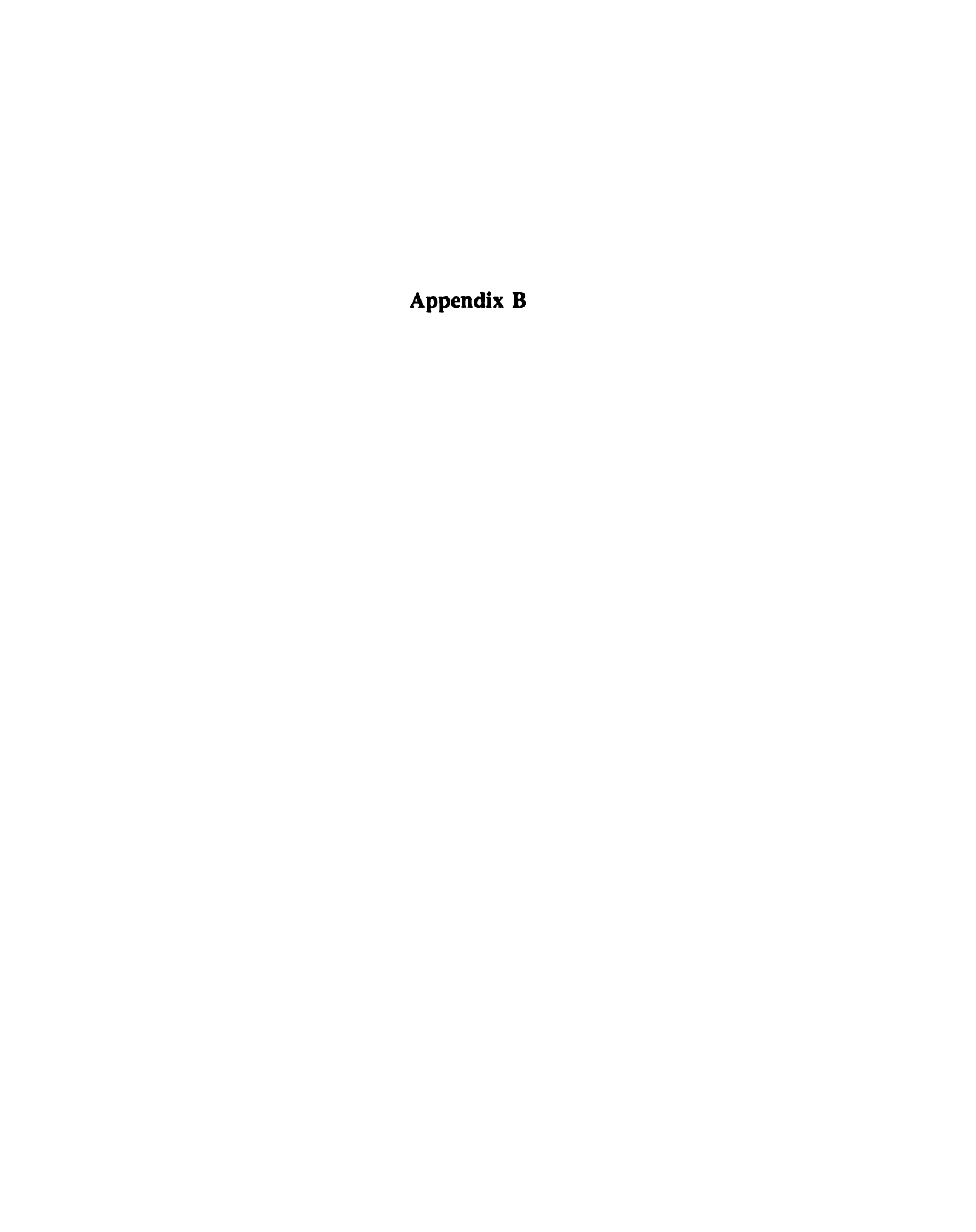


Figure A2 Pendulum impacts, angular velocity vs. time



Appendix B

The Derivation of the Rest Solution Limit

This development shows the conditions for the existence of the rest solution of the inverted pendulum system. A free body diagram is given in Figure B1. Summing moments about the point O yields

$$\sum M_O = 0 = mglSin\theta - NlCos\theta + m\ddot{y}lCos\theta$$
 (B1)

where the base motion is

$$y = ACos\omega_{dr}t (B1a)$$

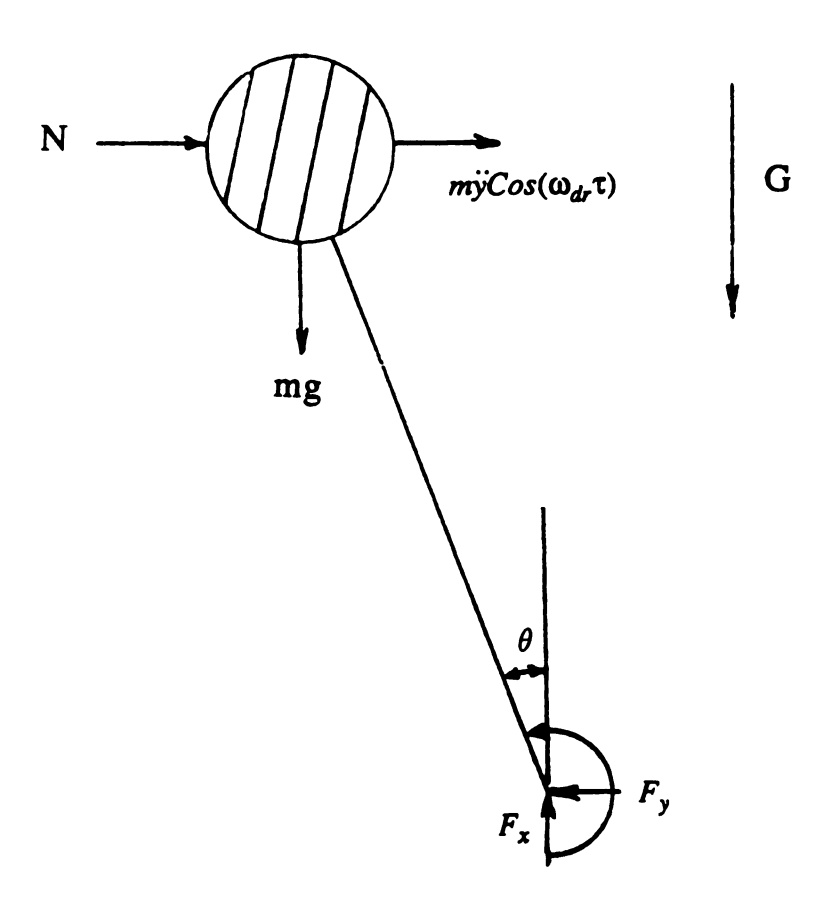


Figure B1 Free body diagram of inverted pendulum at impact

Solving this equation for the normal force, N gives

$$N = \frac{M}{Cos\theta} \left[gSin\theta - A\omega_{dr}^2 Cos\theta Cos\omega_{dr} t \right]$$
 (B2)

For N to remain >0 for all time, we can check its behavior over a single forcing cycle. The worst case is when $Cos\omega_{dr}t = \pm 1$ for the left and right constraint, respectively. The N>0 condition then becomes

$$Sin\theta - \frac{A\omega_{dr}^2}{g} Cos\theta > 0$$
 (B3)

Using the small angle approximations $Sin\theta \approx \theta$ and $Cos\theta \approx 1$, we can reduce B3 to the following equation

$$\theta > \frac{A\omega_{dr}^2}{g} \tag{B4}$$

The nondimensional parameter β is equal to $\frac{A}{\theta_{\max}l}(\omega_{dr}^2/g/l)$. The angle θ is θ_{\max} for this case. This yields the final result

$$\beta < 1$$
 (B5)

This is the parameter values for which the rest solution will exist.

٠



Appendix C

Calibration of the Hall Effect Sensor

The Hall effect sensor is a electronic device which generates an output voltage proportional to the magnetic field near it. Mounting a circular magnet near the sensor will let the sensor produce a voltage proportional to the sine of the angle of the magnet. Since we want a linear relationship between voltage and pendulum displacement, the portion of the sine curve where the sine of the angle is approximately equal to the angle will be used. This provides a sensor whose output is nearly linear.

The sensor was calibrated by fixing the pendulum displacement and recording the resulting output voltage. This was done for various pendulum positions over the maximum range used in the experiment. The measuring voltmeter had an error of 1% and the pendulum position measuring device (a ruler) had an error of about 1% over the range measured. These errors show as the uncetainty boxes on the plot of voltage vs. displacement of the Hall effect sensor (Figure C1). The line fit through these points by a linear regression method had a regression coefficient of 0.99. The calibration constant was determined to be 0.13 mV/in or 0.05 mV/cm.

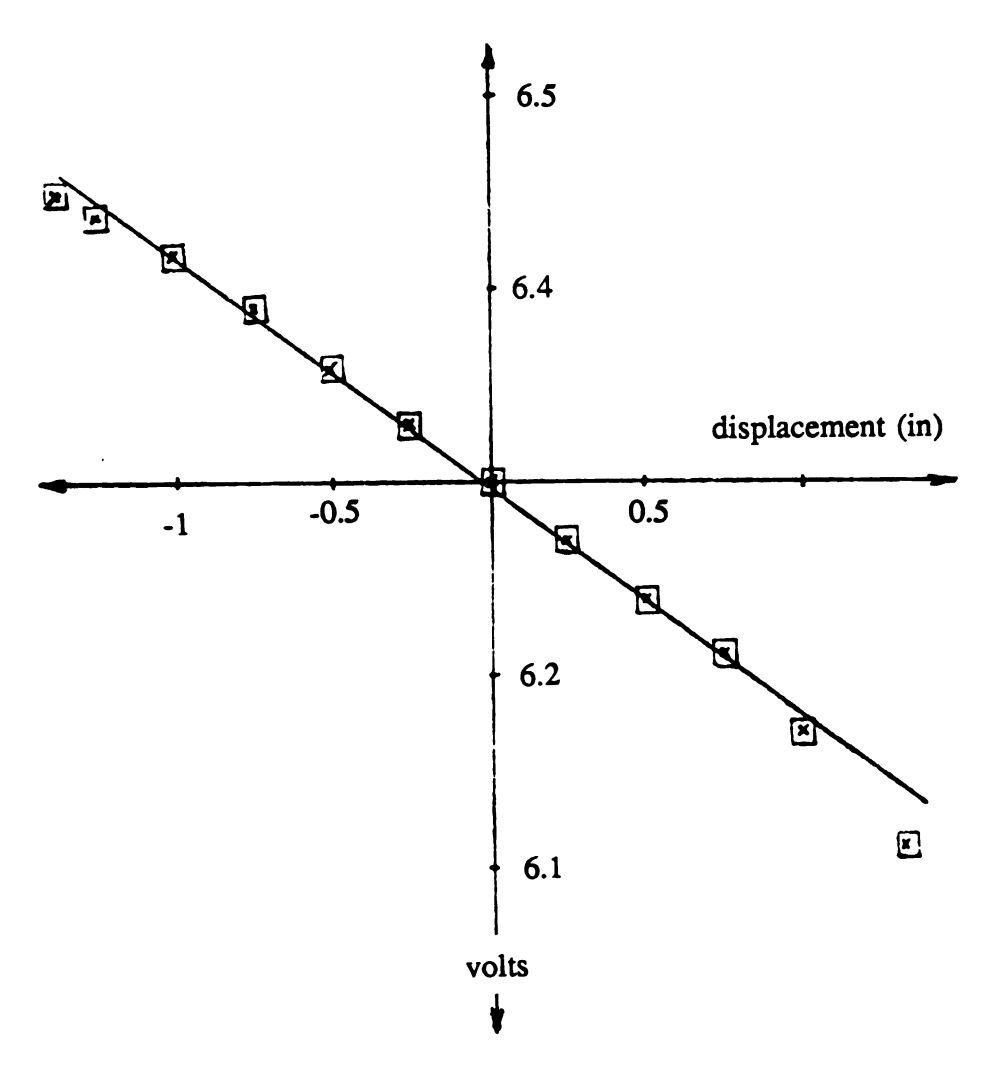


Figure C1 Rotational Sensor Calibration Curve

References

- [1] Shaw, Steven W., "The Transition to Chaos in a Simple Mechanical System", Preprint, Michigan State University 1987.
- [2] Shaw, Steven W., "The Dynamics of a Harmonically Excited System Having Rigid Amplitude Constraints, Part 1: Subharmonic Motions and Local Bifurcations", Transactions of the ASME Journal of Applied Mechanics, Vol. 52 1985, pp. 453-458.
- [3] Shaw, Steven W., "The Dynamics of a Harmonically Excited System Having Rigid Amplitude Constraints, Part 2: Chaotic Motions and Global Bifurcations", Transactions of the ASME Journal of Applied Mechanics, Vol. 52 1985, pp. 459-464.
- [4] Hirsch, Morris W., and Smale, Steven, Differential Equations, Dynamical Systems, and Linear Algebra, Academic Press, Inc. Orlando, Florida, 1974.
- [5] Guckenheimer, John, and Holmes, Phillip, Nonlinear Oscillations, Dynamical Systems, and Bifurcations of Vector Fields, Springer-Verlag, New York, Berlin, Heidelberg, Tokyo, 1983.
- [6] Peitgen, Heinz-Otto, and Richter, Peter H., The Beauty of Fractals, Images of Complex Dynamical Systems, Springer-Verlag, New York, Berlin, Heidelberg, Tokyo, 1986.
- [7] Veluswami, M.A., and Crossley, F.R.E., "Multiple Impacts of a Ball Between Two Plates, Part 1: Some Experimental Observations", Transactions of the ASME Journal of Engineering for Industry, August 1975, pp. 820-827.
- [8] Veluswami, M.A., Crossley, F.R.E, and Horvey, G., "Multiple Impacts of a Ball Between Two plates, Part 2: Mathematical Modelling", Transactions of the ASME Journal of Engineering for Industry, August 1975, pp.828-835.
- [9] Masri, S.F., "Theory of the Dynamic Vibration Neutralizer With Motion Limiting Stops", Transactions of the ASME Journal of Applied Mechanics, June 1972, pp. 563-568.
- [10] Davies, H.G., "Random Vibration of a Beam Impacting Stops", Journal of Sound and Vibration, 1980 68(4), pp. 479-487.
- [11] Watanabe, Takeshi, "Forced Vibration of Nonlinear System with Symmetrical Piecewise-Linear Characteristics", *Bulletin of JSME*, Vol. 27, No. 229, July 1984.
- [12] Watanabe, Takeshi, "Steady Impact Vibrations of Continuous Elements (Case of Colliding Once in a Half Cycle)", Bulletin of JSME, Vol. 24, No. 187, January 1981.
- [13] Moon, Francis C., and Shaw, Steven W., "Chaotic Vibrations of a Beam With Non-Linear Boundary Conditions", *Int. J. of Non-Linear Mechanics*, Vol 18, No.6, pp. 465-477, 1983.
- [14] Shaw, S.W., and Holmes, P.J., "A Periodically Forced Piecewise Linear Oscillator", Journal of Sound and Vibration, (1983) 90(1), pp. 129-155.
- [15] Holmes, P.J., "The Dynamics of Repeated Impacts with a Sinusoidally Vibrating Table", Journal of Sound and Vibration, 84, pp. 173-189, 1982.

- [16] Sharif-Bakhtiar, M., and Shaw, S. W., "The Dynamic Analysis of a Centrifugal Pendulum Vibration Absorber With Motion Limiting Stops", To appear, Midwest Mechanics Conference, September 1987.
- [17] Moon, F.C. and Holmes, P.J., "A Magnetoelastic Strange Attractor", Journal of Sound and Vibration, 65(2), pp 285-296, 1979.
- [18] Moon, F.C., Cusumano, J, and Holmes, P.J., "Evidence for Homoclinic Orbits as a Precursor to Chaos in a Magnetic Pendulum", *PhysicaD*, To Appear
- [19] Shaw, S.W., "Forced Vibrations of a Beam with One-sided Amplitude Constraint: Theory and Experiment", *Journal of Sound and Vibration*, 99(2), .pp 199-212, 1985.
- [20] Carr, J., Applications of Centre Manifold Theory, Springer-Verlag, New York, 1981.
- [21] Feigenbaum, M.J., "Quantitative Universality for a Class of Nonlinear Transformations", Journal of Statistical Physics, 19, pp 25-52, 1978.
- [22] Meirovitch, Leonard, Analytical Methods in Vibrations, The Macmillan Company, New York 1967.

